

SANDIA REPORT

SAND2013-7956
Unlimited Release
September 2013

Electrical Conductivity in Oxygen-Deficient Phases of Transition Metal Oxides from First-Principles Calculations

Robert J. Bondi, Michael P. Desjarlais, Aidan P. Thompson, Geoff L. Brennecka, and Matt Marinella

Prepared by
Sandia National Laboratories
Albuquerque, New Mexico 87185 and Livermore, California 94550

Sandia National Laboratories is a multi-program laboratory managed and operated by Sandia Corporation, a wholly owned subsidiary of Lockheed Martin Corporation, for the U.S. Department of Energy's National Nuclear Security Administration under contract DE-AC04-94AL85000.

Approved for public release; further dissemination unlimited.



Issued by Sandia National Laboratories, operated for the United States Department of Energy by Sandia Corporation.

NOTICE: This report was prepared as an account of work sponsored by an agency of the United States Government. Neither the United States Government, nor any agency thereof, nor any of their employees, nor any of their contractors, subcontractors, or their employees, make any warranty, express or implied, or assume any legal liability or responsibility for the accuracy, completeness, or usefulness of any information, apparatus, product, or process disclosed, or represent that its use would not infringe privately owned rights. Reference herein to any specific commercial product, process, or service by trade name, trademark, manufacturer, or otherwise, does not necessarily constitute or imply its endorsement, recommendation, or favoring by the United States Government, any agency thereof, or any of their contractors or subcontractors. The views and opinions expressed herein do not necessarily state or reflect those of the United States Government, any agency thereof, or any of their contractors.

Printed in the United States of America. This report has been reproduced directly from the best available copy.

Available to DOE and DOE contractors from

U.S. Department of Energy
Office of Scientific and Technical Information
P.O. Box 62
Oak Ridge, TN 37831

Telephone: (865) 576-8401
Facsimile: (865) 576-5728
E-Mail: reports@adonis.osti.gov
Online ordering: <http://www.osti.gov/bridge>

Available to the public from

U.S. Department of Commerce
National Technical Information Service
5285 Port Royal Rd.
Springfield, VA 22161

Telephone: (800) 553-6847
Facsimile: (703) 605-6900
E-Mail: orders@ntis.fedworld.gov
Online order: <http://www.ntis.gov/help/ordermethods.asp?loc=7-4-0#online>



SAND2013-7956
Unlimited Release
September 2013

Electrical Conductivity in Oxygen-Deficient Phases of Transition Metal Oxides from First-Principles Calculations

Robert J. Bondi
Radiation Effects Research Department

Michael P. Desjarlais
Pulsed Power Sciences Center

Aidan P. Thompson
Scalable Algorithms Department

Geoff L. Brenneka
Electronic Materials and Nanostructures Department

Matt Marinella
Radiation Hard CMOS Technology and Advanced Device Development Department

Sandia National Laboratories
P.O. Box 5800
Albuquerque, New Mexico 87185

Abstract

Density-functional theory calculations, *ab-initio* molecular dynamics, and the Kubo-Greenwood formula are applied to predict electrical conductivity in Ta_2O_x ($0 \leq x \leq 5$) as a function of composition, phase, and temperature, where additional focus is given to various oxidation states of the O monovacancy (V_O^n ; $n=0,1+,2+$). Our calculations of DC conductivity at 300K agree well with experimental measurements taken on Ta_2O_x thin films and bulk Ta_2O_5 powder-sintered pellets, although simulation accuracy can be improved for the most insulating, stoichiometric compositions. Our conductivity calculations and further interrogation of the O-deficient Ta_2O_5 electronic structure provide further theoretical basis to substantiate V_O^0 as a donor dopant in Ta_2O_5 and other metal oxides. Furthermore, this dopant-like behavior appears specific to neutral V_O cases in both Ta_2O_5 and TiO_2 and was not observed in other oxidation states. This suggests that reduction and oxidation reactions may effectively act as donor activation and deactivation mechanisms, respectively, for V_O^0 in transition metal oxides.

ACKNOWLEDGMENTS

This work was funded under LDRD Project Number 158699 and Title "Atomistic Modeling of Memristive Switching Mechanisms in Transition Metal Oxides". We thank Mia Blea for fabrication and characterization of Ta₂O₅ pellets and Jim Stevens for sputter deposition of the Ta₂O_x thin films. Barney Doyle, Michael Brumbach, and Andrew Lohn are also appreciated for their contributions to experimental characterization of the Ta₂O_x thin film stoichiometries.

CONTENTS

1. Introduction.....	11
2. Computational Methods.....	15
2.1. Structure Generation.....	15
2.1.1. BCC Ta Derivatives.....	17
2.1.2. Crystalline Ta ₂ O ₅ Derivatives.....	18
2.1.3. Amorphous Ta Derivatives.....	20
2.1.4. Amorphous Ta ₂ O ₅ and TiO ₂ derivatives.....	22
2.2. Conductivity Calculations.....	22
2.2.1. Optical Conductivity.....	22
2.2.2. Sampling and Averaging.....	23
2.2.3. DC Extrapolation and Fitting.....	24
3. Experimental Methods.....	27
4. Crystalline Monovacancy Stability.....	29
5. Electrical Conductivity.....	33
5.1. Metallic Ta.....	34
5.2. Amorphous Ta ₂ O _x	35
5.3. Crystalline Ta ₂ O _x	38
5.4. Amorphous TiO _x	40
6. Electronic Structure.....	43
6.1. Band Gaps.....	43
6.2. Density of States.....	43
6.3. Electron Localization Function.....	46
7. Statistical Variation of Conductivity.....	47
8. Conclusions.....	51
9. References.....	53
Distribution	56

FIGURES

Figure 2.1. Structural views from three perspectives of 168-atom expansion of *c*-Ta₂O₅ Ramprasad [2,3] model. Tantalum and oxygen atoms are represented by light blue and red spheres, respectively. Exemplary “equatorial” cross-sections of the pentagonal bipyramidal (TaO₇) and octahedral (TaO₆) repeat units are shaded in grey. Note the inherent distortion typical of *c*-Ta₂O₅ models evidenced by undrawn, long Ta-O bonds and the categorization of O sites within the z plane in (c).....19

Figure 2.2 Total radial distribution functions characterizing the amorphous structure of (a) *a*Ta160, (b) *a*Ta152O8, (c) *a*Ta144O16, (d) *a*Ta112O48, (e) *a*Ta80O80, (f) *a*Ta48O96, (g) *a*Ta48O108, and (h) *a*Ta48O120 compositions of *a*-Ta₂O_x. Each RDF is an average over 14 MD configuration snapshots. Insets show the first configuration snapshot after 1.5 ps equilibration at 300K. Tantalum and oxygen atoms are represented by light blue and red spheres, respectively. Significant peaks are annotated by the corresponding interaction pair.....21

Figure 2.3. Diversity of 300K optical conductivity responses up to 1 eV as a function of composition in the Ta_2O_x ($0 \leq x \leq 5$, neutral V_O) system. (a)-(c) $\sigma(\omega)$ curves calculated with PBE functionals represent the arithmetic average over 12-14 MD configuration snapshots. (d)-(e) $\sigma(\omega)$ curves calculated with HSE06 functionals represent log averages over at least 6 MD configuration snapshots.....25

Figure 4.1. Configurations of bulk $c\text{-Ta}_2\text{O}_5$ and the monovacancy in various charge states (left) with corresponding ELF contours (right). Tantalum and oxygen atoms are represented by light blue and red spheres, respectively, while dark grey spheres in (a) indicate O lattice sites for V_O creation. Provided measurements (\AA) indicate separation of neighboring Ta atoms near V_O sites. Qualitative interpretation of ELF values: 1.0 represents perfect localization, 0.5 represents metallic regions of free electron gas, and 0.0 represents regions of zero electron density. Coordinate axes apply to both structural configurations and ELF contour plots; however, the view axis that is skewed off-axis for structure depth perspective is parallel to the reader's view in the ELF contours.....30

Figure 4.2. Total energy distributions of the $c\text{-Ta}_2\text{O}_5$ monovacancy in three charge states in 168-atom supercells. Jitter was added to the horizontal axis for visual clarity. For each charge state, a minimum of 5 configurations were sampled from each O site category (21 total configurations). The lowest energy for each charge state is the representative configuration used for property calculations.....31

Figure 5.1. Correlation of DC conductivities at 300K for $a\text{-Ta}_2\text{O}_x$ ($0 \leq x \leq 5$, neutral V_O) calculated from DFT calculations (solid shapes) for both PBE and HSE06 functionals with experimental conductivity measurements (open shapes) on both Ta_2O_x ($0.18 \leq x \leq 4.72$) thin films and air- and O_2 -sintered bulk Ta_2O_5 pellets. DFT σ_0 values are those represented in Table 2.1.....33

Figure 5.2. Optical conductivities contrasting the temperature dependence by phase in 160-atom supercells of (a) BCC Ta and (b) amorphous Ta. All $\sigma(\omega)$ curves represent the arithmetic average over 14 MD configuration snapshots. Spatial components $\sigma_{xx}(\omega)$, $\sigma_{yy}(\omega)$, $\sigma_{zz}(\omega)$ are identical through BCC symmetry and therefore averaged.....35

Figure 5.3. Optical conductivity curves at 10 temperatures in near-stoichiometric compositions of $a\text{-Ta}_2\text{O}_x$ in 168-atom basis supercells. $\sigma(\omega)$ for $a\text{-Ta}_2\text{O}_5$ calculated with (a) PBE and (b) HSE06 functionals. $\sigma(\omega)$ calculated with HSE06 functionals for (c) V_O^0 , (d) V_O^{1+} , and (e) V_O^{2+} in $a\text{-Ta}_2\text{O}_5$. $\sigma(\omega)$ curves calculated with PBE functionals represent the arithmetic average over a minimum 14 MD configuration snapshots, while $\sigma(\omega)$ curves calculated with HSE06 functionals represent the log average over a minimum 6 MD configuration snapshots.....37

Figure 5.4. Optical conductivities at 300K for near-stoichiometric compositions of $a\text{-Ta}_2\text{O}_5$ with V_O^n in various charge states ($n = 0, 1+, 2+$). The thick grey line references $\sigma(\omega)$ for stoichiometric $a\text{-Ta}_2\text{O}_5$. All $\sigma(\omega)$ curves represent the log average over a minimum 6 MD configuration snapshots.....38

Figure 5.5. Optical conductivity curves at seven temperatures in near-stoichiometric compositions of $c\text{-Ta}_2\text{O}_x$ in 168-atom basis supercells. $\sigma(\omega)$ are shown only for zz normal components ($\sigma_{zz}(\omega)$) calculated with HSE06 functionals for (a) bulk $c\text{-Ta}_2\text{O}_5$, (b) V_O^0 , (c) V_O^{1+} , and (d) V_O^{2+} . All $\sigma(\omega)$ curves represent the log average over a minimum 6 MD configuration snapshots.....39

Figure 5.6. Optical conductivities for three normal components in bulk c -Ta₂O₅ calculated with HSE06 functionals at (a) 300K and (b) 1000K. All $\sigma(\omega)$ curves represent the log average over a minimum 6 MD configuration snapshots.....40

Figure 5.7. Optical conductivities at 300K for near-stoichiometric compositions of a -TiO₂ with V_Oⁿ in various charge states (n = 0, 1+, 2+). The thick grey line references $\sigma(\omega)$ for stoichiometric a -TiO₂. All $\sigma(\omega)$ curves represent the log average over 10 to 14 MD configuration snapshots.....41

Figure 5.8. Optical conductivity curves at various temperatures in near-stoichiometric compositions of a -TiO_x in 216-atom basis supercells. $\sigma(\omega)$ calculated with HSE06 functionals for (a) a -TiO₂, (b) V_O⁰ in a -TiO₂, and (c) V_O²⁺ in a -TiO₂. All $\sigma(\omega)$ curves represent the log average over 10 to 14 MD configuration snapshots.....42

Figure 6.1. Total density of states for eight compositions of a -Ta₂O_x where each figure represents one MD configuration snapshot at 300K. Vertical, dashed blue lines reference the Fermi level for each configuration. A reference TDOS is shown in (a) for a -Ta₂O₅, while the effect of the monovacancy in three charge states is shown in (b) V_O⁰, (c) V_O¹⁺, and (d) V_O²⁺. The cumulative effect of additional neutral V_O on TDOS is shown in (e) 2V_O, (f) 3V_O, (g) 6V_O, and (h) 12V_O.....45

Figure 7.1. Statistical evolution of optical conductivity response for aTa48O119 (V_O⁰) as a function of temperature. Six $\sigma(\omega)$ curves calculated from HSE06 functionals at each temperature correspond to six MD configuration snapshots taken at 0.5 ps intervals.....47

Figure 7.2. Statistical distributions sampling temporal variation of DC conductivity for (a) BCC Ta and (b) aTa48O119 (V_O⁰) from sampling 94 MD configuration snapshots at 0.5 ps intervals at 500K. (a) σ_0 determined with PBE functionals and blue line represents arithmetic average. (b) σ_0 determined with HSE06 functionals and blue line represents log average. Three outliers represents the minimum non-zero $\sigma(\omega > 0)$ yielded in simulation. (c) Statistical distribution of σ_0 for aTa48O119 (V_O⁰) from sampling 14 MD configuration snapshots across 10 different amorphous samples (140 total samples) at 500K using HSE06 functionals.....48

TABLES

Table 2.1. Electrical conductivity summary for amorphous Ta₂O_x structures. Structure names quantify constituent atomic species in each supercell. Calculations using HSE06 functionals sample at least 6 MD configuration snapshots, while PBE calculations sample 12 to 14 MD configuration snapshots. Band gap uncertainties are standard deviations. σ_0 values are extrapolated from either arithmetic or log averages of sampled $\sigma(\omega)$ data depending on group (see text for details).....16

Table 2.2. Electrical conductivity summary for crystalline Ta₂O_x structures. Structure names quantify constituent atomic species in each supercell. Calculations using HSE06 functionals sample at least 6 MD configuration snapshots, while PBE calculations sample 14 MD configuration snapshots. Band gap uncertainties are standard deviations. σ_0 values are extrapolated from arithmetic averages of sampled $\sigma(\omega)$ data for BCC Ta, while σ_0 values are extrapolated from log averages of sampled $\sigma(\omega)$ data for the three normal components in c -Ta₂O₅ derivative structures (see text for details).....17

Table 6.1. Computed Ta₂O₅ band gaps as a function of temperature calculated with HSE06 functionals. Values represent averages over a minimum of 6 MD configuration snapshots with uncertainties provided as standard deviations.....43

NOMENCLATURE

AC	alternating current
BCC	body-centered cubic
BZ	Brillouin zone
CBM	conduction band minimum
CMOS	complementary metal oxide semiconductor
CN	coordination number
DC	direct current
DFT	density-functional theory
DOS	density of states
ELF	electron localization function
E_g	band gap energy
GGA	generalized gradient approximation
HSE	Heyd, Scuseria, and Ernzerhof
MD	molecular dynamics
MIT	metal-insulator-transition
MO _x	metal oxide
MP	Monkhorst-Pack
NN	nearest neighbor
PAW	projector-augmented wave
PBC	periodic boundary condition
PBE	Perdew, Burke, and Ernzerhof
RBS	Rutherford backscattering
RDF	radial distribution function
QMD	quantum molecular dynamics
SR	Stephenson and Roth
TCR	thermal coefficient of resistance
TMO	transition metal oxide
VASP	Vienna <i>ab-initio</i> simulation program
VBM	valence band maximum
V _O	oxygen vacancy
VR	volume relaxation
XPS	X-ray photoelectron spectroscopy
$\epsilon(\omega)$	dielectric function
$\sigma(\omega)$	optical or AC conductivity
σ_0	DC conductivity
ω	frequency

This page intentionally left blank.

1. INTRODUCTION

Recent interest in tantalum pentoxide (Ta_2O_5) is motivated by new technological applications including optical coatings [1], high-k dielectrics [2,3], and memristive devices [4-8] for constructing resistive random access memories (ReRAM). A memristor is a two-terminal, passive circuit element in which the resistance is modulated by the integral of charge passed in a reversible, hysteretic fashion. While the first physical memristor implementation was reported in 2008 in TiO_2 [9,10] and numerous metal oxides (MO_x) [11-14] have since been used to demonstrate memristive behavior, Ta_2O_x is currently the most promising memristor candidate material. In MO_x memristors, the O vacancy (V_O) is thought to be the essential mediator of conduction, somewhat analogous to the essential role of the dopant atom in semiconductors that is the basis for transistor operation. Early Ta_2O_x memristor performance metrics including high endurance (over 10^{12} cycles) [6], fast switching (< 10 ns) [4], low energy (~ 1 pJ/operation) [4], and scalability [4] make high-density memristor arrays promising candidates to supplant established Flash, SRAM, and DRAM technologies as ubiquitous, non-volatile memories compatible [15] with conventional complementary metal oxide semiconductor (CMOS) processes. An improved understanding of Ta_2O_5 , especially in the context of a reduced metal oxide, is essential to enable practical application in emerging technologies.

Experimental studies in Ta_2O_x materials are largely confined to metallic Ta and the stoichiometric oxide, Ta_2O_5 , leaving details about the intermediate oxygen-deficient compositions virtually unexplored. Pure Ta metal crystallizes in the body-centered cubic structure (BCC) which makes *c*-Ta the best-defined reference point in the Ta-O system. Experimental data for amorphous Ta (*a*-Ta) also exists in the thin film context because of its relevance in microelectronic applications [16,17]. Since high-k capacitor dielectrics are the most common application of Ta_2O_5 to date, many studies in recent years focused on the breakdown and leakage characteristics of *a*- Ta_2O_5 to assess the feasibility of incorporation in integrated circuit manufacturing. The work of Fleming *et al.* [18] concluded that O vacancy (V_O) defect concentrations near metal-oxide interfaces are an essential contributor to spurious Ta_2O_5 leakage currents, while Iosad *et al.* [19] attributed the variability in dielectric response of several transition metal oxides (TMOs), including Ta_2O_5 , to a dopant-like behavior that depends on the concentration of quenched-in vacancies. Nakamura *et al.* [20] provided one of the first studies of V_O aggregation, which is likely an essential mechanism of conductivity modulation.

Recent interest in optical properties and potential memristor applications has fueled experimental characterization of intermediate, O-deficient compositions for numerous TMOs. Gnanarajan *et al.* [21] studied reduced Ta_2O_5 for application of Ta_2O as a transparent, conducting film. Goldfarb *et al.* [22] provided an extensive study of the electronic structure and possible conduction mechanisms in TMOs, including *a*- Ta_2O_x , and found that all amorphous films displayed Fermi glass behavior. Their findings also suggest that *a*- Ta_2O_x provides the best binary TMO system to exhibit a continuously variable degree of electron localization and therefore the best opportunity to tune conduction as a function of *x*. Similarly, the binary simplicity of the ambient Ta-O phase diagram [23] is widely-cited as the explanation for the good repeatability and endurance characteristics of Ta_2O_x memristors for basic ON/OFF operation.

Despite the simplicity of the Ta-O phase diagram, the crystal structure of Ta₂O₅ remains a subject of current debate [23-25] and obfuscates the natural entry point to an atomistic study of simple point defects. The difficulty inherent in fully equilibrating a multitude of nearly degenerate atomistic configurations obscures computational determination of the crystalline Ta₂O₅ (*c*-Ta₂O₅) primitive cell and ambient growth of Ta₂O₅ crystals is similarly impractical; consequently, the lingering structural ambiguity surrounding *c*-Ta₂O₅ leaves the exact crystal structure itself predominantly a theoretical discussion. Ta₂O₅ is known to commonly exhibit two polymorphs: low-temperature Ta₂O₅ (L-Ta₂O₅ or β -Ta₂O₅) and high-temperature Ta₂O₅ (H-Ta₂O₅ or α -Ta₂O₅), where the temperature transition is ~ 1360 °C [23,24]. While generally less used, there are also studies claiming a hexagonal, low-temperature form of Ta₂O₅, δ -Ta₂O₅ [26]; however, variants of the orthorhombic, low-temperature Ta₂O₅ structural model of Stephenson and Roth [27] prevail in the literature. The basic building blocks for the Stephenson and Roth *c*-Ta₂O₅ model are distorted TaO₆ octahedra and TaO₇ pentagonal bipyramids in which the central Ta cations are arranged in sheets. The idealized Stephenson and Roth (SR) unit cell has Ta₂₂O₅₈ stoichiometry, but concepts of partial O occupancy and distortion planes are introduced that reduce the coordination number (CN) for three Ta cations from seven to six in each unit cell and yield an overall stoichiometry of Ta₂₂O₅₅ [27, 28].

The existing literature contains a limited amount of computational work on Ta₂O₅ and a number of different crystalline structural models. The apparent lack of an interatomic potential for Ta-O precludes immediate investigation with classical molecular dynamics (MD); therefore, most computational work is relegated to first-principles density-functional theory (DFT) studies. Sawadi and Kawakami [28] used DFT methods on a derivative of the SR model and concluded that V_O defect levels in the band gap are responsible for leakage currents and that V_O act as donors for conduction. Ramprasad [2,3] used a 14-atom simplification of the SR unit cell to study V_O energetics and migration in various charge states and demonstrated the significance of local structure in Ta₂O₅, rather than long-range order and crystal symmetry. He found both neutral (V_O⁰) and 2+ V_O (V_O²⁺) to be the most stable and determined the polyhedral “cap” sites might kinetically behave as O vacancy sinks. Andreoni and Pignedoli [29] used first-principles calculations to find that interpolyhedral vibrations are largely responsible for dielectric constant variations between polymorphs. Wu *et al.* [30] used DFT to study the structure and mechanical properties of four *c*-Ta₂O₅ structures as well as an amorphous Ta₂O₅ structure constructed with a Monte Carlo (MC) method. Bassiri *et al.* [1] produced *a*-Ta₂O₅ models using a combination of reverse MC and *ab-initio* MD that showed both no structural order beyond the second nearest neighbor (NN) and evidence that the limited short-range order observed was the contribution of Ta₂O₂ ring fragments, consistent with sputter deposition of *a*-Ta₂O₅ thin films. Collectively, the computational efforts on Ta₂O₅ suggest that the local bonding environment, not the long-range order from crystal periodicity, contains the essential electronic structure details to reproduce critical observables; as a result, the necessity of a universally-accepted crystal unit cell for the first-principles study of defects in *c*-Ta₂O₅ is diminished.

In this paper, we extend first-principles methods based on the Kubo-Greenwood formula [31-33] and often applied in metallic regimes [34-40] to calculate electrical conductivity as a function of phase, composition, and temperature across the full spectrum of Ta₂O_x materials, where

additional focus is given to the monovacancy in various charge states. In particular, we apply a melt-and-quench strategy with *ab-initio* MD to first construct a set of amorphous Ta_2O_x ($0 \leq x \leq 5$) structures quenched to at least three different temperatures ($T = 300, 500, \text{ and } 1000\text{K}$). The endpoint crystalline compositions are represented by BCC Ta and a volume-relaxed version of the Ramprasad *c*- Ta_2O_5 model. Ta_2O_x thin films and bulk Ta_2O_5 pellets were also generated in the laboratory and their conductivity measurements are compared with DFT conductivity predictions. DFT calculations of electronic structure are also presented for calculated band gaps and defect levels derived from density of states (DOS) and the electron localization function (ELF) surrounding various states of the monovacancy. In addition, a statistical treatment of Ta_2O_x conductivity is provided through analysis of spatial, temporal, and structural contributions to direct current (DC) conductivity (σ_0). Our electrical conductivity calculations in Ta_2O_x provide both valuable insight into the substoichiometric phases of Ta_2O_5 while also providing a general approach to extending established first-principles conductivity methods into semiconducting and insulating systems.

This page intentionally left blank.

2. COMPUTATIONAL METHODS

All atomistic configurations, electronic structures, and conductivity calculations reported herein were computed using a plane-wave pseudopotential method within the generalized gradient approximation (GGA) to DFT [41], as implemented in the Vienna *ab-initio* simulation package (VASP) [42]. Projector-augmented wave (PAW) pseudopotentials [43], which in principle comprise an all-electron frozen-core approach that represent exact valence wave functions, were employed throughout this work. The exchange-correlation functional of Perdew, Burke, and Ernzerhof (PBE) [44] evaluated in GGA is used throughout this work, while some calculations are additionally refined with the hybrid functional of Heyd, Scuseria, and Ernzerhof (HSE06) [45,46] to correct the band gap (E_g) and improve the accuracy of conductivity calculations in various insulating compositions of Ta_2O_x . All calculations in this work were performed with Ta PAW pseudopotentials with $5d^36s^2$ valence configuration and the soft O PAW pseudopotential with $2s^22p^4$ valence configuration. The 11 electron Ta PAW and harder O PAWs were also checked, but found to have a negligible effect on resulting conductivity calculations. Various charge states of $\text{V}_\text{O}^\text{n}$ were simulated in the context of a neutralizing background jellium as implemented in VASP.

Convergence of DFT results with respect to cutoff energy, kpoint mesh, supercell size, and number of empty conduction bands were studied separately for *c*-Ta and *c*- Ta_2O_5 and optimized parameters were applied accordingly to all derivative structures from each parent. Full convergence with respect to cell size was found to be impractical for either endpoint composition, consistent with other first-principles conductivity studies [35,36]. For the 160-atom supercell of *c*-Ta, the estimated error in DC conductivity, σ_0 , is approximately 30% overestimation to tabulated reference values [47], while even estimation of the error is more elusive for *c*- Ta_2O_5 because no well-defined reference material exists.

An iterative, DFT-based volume relaxation (VR) procedure was regularly used throughout this work to help ensure the lowest energy structures were used for property calculations. Our iterative VR approach alternates between adjustment of supercell volume and relaxation of the constituent ions until the DFT convergence criteria are achieved. The lack of a well-defined structure for *c*- Ta_2O_5 , and consequently associated lattice constants, motivated VR as a general tool to optimize the supercell. In a previous work, Bondi *et al.* [48] demonstrated the utility of sample-specific VR when working with sets of independently-derived amorphous structures. In addition, iterative VR was applied during all QMD quenching stages to help compensate for density changes resulting from large temperature changes.

2.1. Structure Generation

The conditions for DFT calculations were optimized separately for structures derived from metallic Ta and structures derived from Ta_2O_5 . Tables 2.1 and 2.2 summarize the structures studied in this work, while the following sections categorize the structures into four groups and detail the computational methods applied to each. *Ab-initio* MD simulation, also known as finite-temperature DFT-MD (FT-DFT-MD) or quantum MD (QMD), was used extensively in

this work both for amorphous structure generation and for temporal sampling of ionic configuration snapshots as an essential step to first-principles conductivity calculations.

Table 2.1. Electrical conductivity summary for amorphous Ta₂O_x structures. Structure names quantify constituent atomic species in each supercell. Calculations using HSE06 functionals sample at least 6 MD configuration snapshots, while PBE calculations sample 12 to 14 MD configuration snapshots. Band gap uncertainties are standard deviations. σ_0 values are extrapolated from either arithmetic or log averages of sampled $\sigma(\omega)$ data depending on group (see text for details).

structure	Ta ₂ O _x				E _g (eV)		log ₁₀ σ_0 ($\Omega^{-1}\text{m}^{-1}$)				
	x	O%	V _O %	charge	300K		500K		1000K		
					HSE06	PBE	HSE06	PBE	HSE06	PBE	HSE06
group 1											
α Ta160	0.00	0.0	n/a	0		5.94		5.98		6.03	
α Ta160O1	0.01	0.6	n/a	0		5.98					
α Ta160O2	0.03	1.2	n/a	0		5.99					
α Ta160O3	0.04	1.8	n/a	0		5.94					
group 2											
α Ta152O8	0.11	5.0	n/a	0	no gap	5.92	5.16	5.93	5.38	5.99	5.64
α Ta144O16	0.22	10.0	n/a	0	no gap	5.91	5.14	5.93	5.42	5.99	5.63
α Ta128O32	0.50	20.0	n/a	0	no gap	5.80	4.83	5.86	5.19	5.89	5.52
α Ta112O48	0.86	30.0	n/a	0	no gap	5.69	4.75	5.73	5.08	5.79	5.42
α Ta96O64	1.33	40.0	n/a	0	no gap	5.60	4.06	5.62	4.93	5.65	5.27
α Ta80O80	2.00	50.0	n/a	0	no gap	5.21	3.97	5.27	4.53	5.39	4.93
α Ta64O96	3.00	60.0	n/a	0	no gap	5.00	3.23	4.52	3.71	4.93	4.41
group 3											
α Ta48O84	3.50	63.6	30.0	0	3.27 ± 1.56	4.14	-0.33	4.22	0.57	4.65	4.24
α Ta48O96	4.00	66.7	20.0	0	3.51 ± 0.10	3.74	-1.43	4.24	2.23	4.51	3.69
α Ta48O108	4.50	69.2	10.0	0	3.76 ± 0.22	3.37	-0.74	3.67	1.45	4.35	3.97
group 4											
α Ta48O114 ^b	4.75	70.4	5.0	0	3.58 ± 0.27		-2.61		3.89		4.32
α Ta48O117	4.88	70.9	2.5	0	3.64 ± 0.15		-5.49		1.14		2.78
α Ta48O117	4.88	70.9	2.5	2+	3.42 ± 0.13		-8.07		-7.18		-3.71
α Ta48O118	4.92	71.1	1.7	0	3.56 ± 0.06		-5.05		3.24		3.94
α Ta48O118	4.92	71.1	1.7	2+	3.45 ± 0.12		-6.82		-7.37		-3.83
α Ta48O119	4.96	71.3	0.8	0	3.67 ± 0.15		a		-7.83		-0.11
α Ta48O119	4.96	71.3	0.8	1+	3.53 ± 0.21		3.63		3.78		3.96
α Ta48O119	4.96	71.3	0.8	2+	3.47 ± 0.12		-7.06		-6.63		-3.70
α Ta48O120	5.00	71.4	0.0	0	3.54 ± 0.09	-6.48	-6.69	-6.80	-6.95	-0.79	-3.59

^aNo finite DC conductivity from simulation

^b300K data samples 4 independent structures

Table 2.2. Electrical conductivity summary for crystalline Ta₂O_x structures. Structure names quantify constituent atomic species in each supercell. Calculations using HSE06 functionals sample at least 6 MD configuration snapshots, while PBE calculations sample 14 MD configuration snapshots. Band gap uncertainties are standard deviations. σ_o values are extrapolated from arithmetic averages of sampled $\sigma(\omega)$ data for BCC Ta, while σ_o values are extrapolated from log averages of sampled $\sigma(\omega)$ data for the three normal components in c-Ta₂O₅ derivative structures (see text for details).

structure	Ta ₂ O _x				E _g (eV)		log ₁₀ σ_o ($\Omega\text{-m}$) ⁻¹				
	x	O%	V _O %	charge	300K HSE06	300K PBE	300K HSE06	500K PBE	500K HSE06	1000K PBE	1000K HSE06
BCC Ta											
<i>c</i> Ta160	0.00	0.0	n/a	0		7.03		6.81		6.58	
<i>c</i> Ta160O1	0.01	0.6	n/a	0		6.91					
<i>c</i> Ta160O2	0.03	1.2	n/a	0		6.84					
$\sigma_{o,xx}$, c-Ta ₂ O ₅											
<i>c</i> Ta48O119	4.96	71.3	0.8	0	3.26 ± 0.13		-26.00		-5.35		-0.70
<i>c</i> Ta48O119	4.96	71.3	0.8	1+	3.34 ± 0.06		3.44		4.31		3.64
<i>c</i> Ta48O119	4.96	71.3	0.8	2+	3.39 ± 0.06		-6.57		-6.27		-3.47
<i>c</i> Ta48O120	5.00	71.4	0.0	0	3.34 ± 0.16		-6.64		-6.55		-3.72
$\sigma_{o,yy}$, c-Ta ₂ O ₅											
<i>c</i> Ta48O119	4.96	71.3	0.8	0	a		-26.03		-5.36		-0.75
<i>c</i> Ta48O119	4.96	71.3	0.8	1+	a		3.62		4.24		3.70
<i>c</i> Ta48O119	4.96	71.3	0.8	2+	a		-6.62		-6.20		-3.58
<i>c</i> Ta48O120	5.00	71.4	0.0	0	a		-7.34		-6.45		-3.72
$\sigma_{o,zz}$, c-Ta ₂ O ₅											
<i>c</i> Ta48O119	4.96	71.3	0.8	0	a		-26.19		-6.10		-1.09
<i>c</i> Ta48O119	4.96	71.3	0.8	1+	a		2.01		3.20		3.40
<i>c</i> Ta48O119	4.96	71.3	0.8	2+	a		-5.01		-5.09		-3.21
<i>c</i> Ta48O120	5.00	71.4	0.0	0	a		-5.41		-5.05		-3.18

^aValues same as xx component, no directional dependence

2.1.1. BCC Ta derivatives

Using a 1-atom supercell, we found the optimized lattice constant for our prototype BCC Ta structure to be 3.321 Å. Using this primitive cell and periodic boundary conditions (PBCs), we expanded this cell to 160 atoms for the results reported in this work. Using the aforementioned iterative volume relaxation procedure, even the *c*-Ta volume was optimized at each equilibration temperature prior to conductivity calculations to enhance consistency with other structures studied. The *c*Ta160O1 and *c*Ta160O2 structures were generated by insertion of O atoms into *c*Ta160 octahedral interstitial sites of the BCC sublattice following the strategy of Udyansky *et al.* [49] applied to interstitial impurities in BCC Fe.

Structural optimization of Ta derivative structures was conducted with planewave cutoff energies of 400 eV, Brillouin zone (BZ) sampling with 5×5×5 Monkhorst-Pack (MP) kpoint grids, Methfessel-Paxton [50] smearing of electron occupancies, and a convergence criterion of 5×10⁻² eV/Å on the residual forces between atoms. Accurate total energy calculations were conducted on optimized structures by increasing the kpoint mesh to a 9×9×9 MP grid, while iterative VR calculations used only Γ -point BZ sampling.

2.1.2. Crystalline Ta₂O₅ derivatives

For the crystalline reference for Ta₂O₅, we started with the 14-atom model of Ramprasad [2,3]. Using PBCs, this model was expanded to 168 atoms (*c*Ta₄₈O₁₂₀) for all *c*-Ta₂O₅ reference results reported in this work. Application of the iterative VR procedure to the orthorhombic Ramprasad model produced the 168-atom supercell depicted in Fig. 2.1 with the following dimensions: $x = 14.635 \text{ \AA}$, $y = 12.377 \text{ \AA}$, and $z = 11.761 \text{ \AA}$. Fig. 2.1 clearly shows several key features of the SR model retained in the Ramprasad model: (1) TaO₆ and TaO₇ polyhedral layers stacked in the *z* direction; (2) “in-plane” or “equatorial” versus “cap” O sites as determined by the *z* coplanar presence or absence of Ta cations; and (3) regions of distortion resulting from VR of the structure.

Structural optimization of Ta₂O₅ derivative structures was conducted with planewave cutoff energies of 300 eV, BZ sampling at the Γ point, Gaussian smearing of electron occupancies, and a convergence criterion of $5 \times 10^{-2} \text{ eV/\AA}$ on the residual forces between atoms. Accurate total energy calculations were conducted on optimized structures by increasing the kpoint mesh to a $2 \times 2 \times 2$ MP grid and the planewave cutoff energy to 400 eV, while iterative VR calculations used only Γ point BZ sampling.

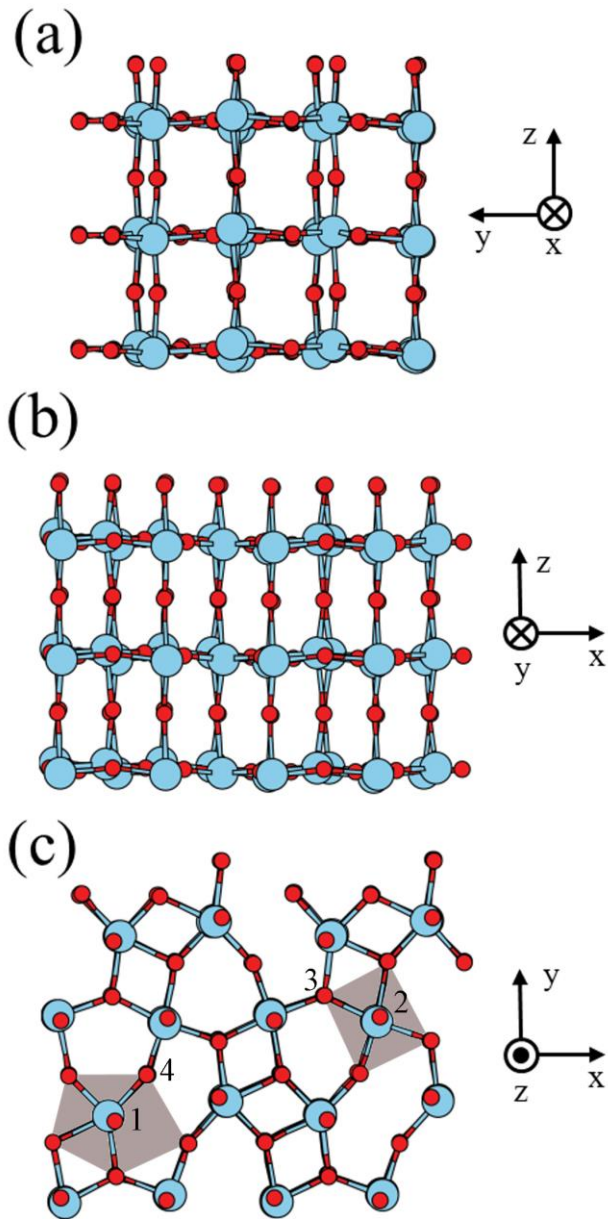


Figure 2.1. Structural views from three perspectives of 168-atom expansion of $c\text{-Ta}_2\text{O}_5$ Ramprasad [2,3] model. Tantalum and oxygen atoms are represented by light blue and red spheres, respectively. Exemplary “equatorial” cross-sections of the pentagonal bipyramidal (TaO_7) and octahedral (TaO_6) repeat units are shaded in grey. Note the inherent distortion typical of $c\text{-Ta}_2\text{O}_5$ models evidenced by undrawn, long Ta-O bonds and the categorization of O sites within the z plane in (c).

2.1.3. Amorphous Ta derivatives

A general temperature profile was developed for the melt-and-quench approach to generation of amorphous Ta derivatives. First, the initial 160-atom *c*-Ta structure was quickly ramped from 0 to 4500K in 2 ps. Then, 4500K was sustained for 20 ps which provided sufficient time to both melt and equilibrate the subsequent liquid phase. The resultant liquid Ta configuration after 22 ps became a common point from which other Ta_2O_x ($0 \leq x \leq 3$) structures were generated through either the addition of O (group 1 in Table 2.1) or the substitution of Ta with O (group 2 in Table 2.1). Following manipulation of the O content, structures were equilibrated for another 6 to 20 ps at 4500K. Next, all structures were quenched to 300K in a 5-step process: (1) VR at 4500K, (2) quench from 4500 to 2400K, (3) VR at 2400K, (4) quench from 2400 to 300K, and (5) VR at 300K. For conductivity calculations, all 300K configuration snapshots were collected from an additional 8 ps of 300K equilibration, while all other temperatures were accommodated by a quick ramp/quench to the target temperature, volume-relaxed at that temperature, then equilibrated for 8 ps at the target temperature for QMD snapshot extraction.

For QMD simulations on Ta derivatives, we used 400 eV cutoff energies, Γ -point sampling, 2 fs step sizes, and an energy convergence tolerance of 1×10^{-3} eV at each QMD step. Methfessel-Paxton smearing was generally used for smearing, but was updated to Fermi smearing for temperature equilibration stages used for conductivity calculations.

Figures 2.2(a)-(e) illustrate representative *a*-Ta derivative structures of *a*- Ta_2O_x generated with this procedure along with their corresponding radial distributions functions (RDFs) to provide a qualitative metric of the evolution of short-range order in our *a*- Ta_2O_x structures as O content increases. The RDF shown at each composition represents the average short-range order at 300K over 14 MD configurations sampled from 1.5 to 8 ps of MD simulation at 0.5 ps intervals. The insets illustrate the first atomistic configuration snapshot after 1.5 ps of 300K equilibration. As the O content is increased, the first Ta NN peak near 3.0 Å decreases, while the Ta-O peak at approximately 2.0 Å increases. These characteristic bond lengths for Ta-Ta and Ta-O are consistent with results from other studies in Ta_2O_5 [1,2,30].

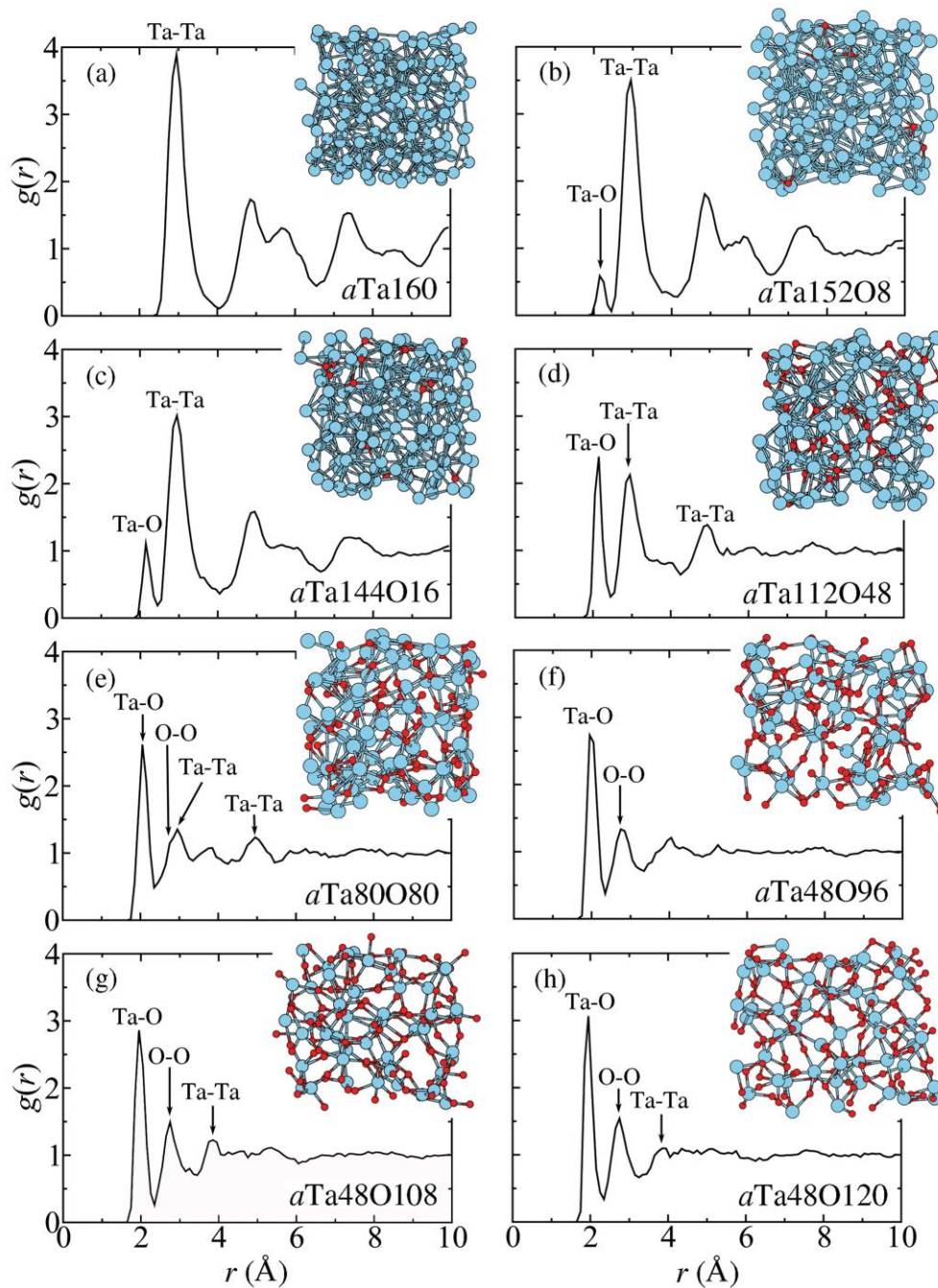


Figure 2.2. Total radial distribution functions characterizing the amorphous structure of (a) $a\text{Ta}_{160}$, (b) $a\text{Ta}_{152}\text{O}_8$, (c) $a\text{Ta}_{144}\text{O}_{16}$, (d) $a\text{Ta}_{112}\text{O}_{48}$, (e) $a\text{Ta}_{80}\text{O}_{80}$, (f) $a\text{Ta}_{48}\text{O}_{96}$, (g) $a\text{Ta}_{48}\text{O}_{108}$, and (h) $a\text{Ta}_{48}\text{O}_{120}$ compositions of $a\text{-Ta}_2\text{O}_x$. Each RDF is an average over 14 MD configuration snapshots. Insets show the first configuration snapshot after 1.5 ps equilibration at 300K. Tantalum and oxygen atoms are represented by light blue and red spheres, respectively. Significant peaks are annotated by the corresponding interaction pair.

2.1.4. Amorphous Ta₂O₅ and TiO₂ derivatives

Another temperature profile was developed for the melt-and-quench approach to generation of amorphous Ta₂O₅ derivatives. A similar melt-and-quench procedure was used to generate amorphous TiO₂ derivative structures from 216-atom basis supercells. First, the initial 168-atom *c*-Ta₂O₅ structure was ramped from 0 to 3900K in 4 ps. Then, 3900K was sustained for 20 ps which provided sufficient time to both melt and equilibrate the subsequent liquid phase. The resultant liquid Ta₂O₅ configuration after 24 ps became a common point from which other Ta₂O_x (3.5 ≤ x ≤ 5) structures were generated through subtraction of O (groups 3 and 4 in Table 2.1). Following reduction of the stoichiometric oxide through O removal, structures were equilibrated for another 6 (10) ps at 3900K for group 4 (3) structures. Next, all structures were quenched to 300K in a 5-step process: (1) VR at 3900K, (2) quench from 3900 to 2100K, (3) VR at 2100K, (4) quench from 2100 to 300K, and (5) VR at 300K. For conductivity calculations, QMD configuration snapshot extraction at the target equilibration temperature follows the method described for Ta derivatives in the previous section.

For QMD simulations on Ta₂O₅ derivatives, we used 300 eV cutoff energies, Γ -point sampling, 2 fs step intervals, and an energy convergence tolerance of 1×10^{-3} eV at each QMD step. Gaussian smearing was generally used for smearing, but was updated to Fermi smearing for the temperature equilibration stages used for conductivity calculations.

Figures 2.2(f)-(h) illustrate representative *a*-Ta₂O₅ derivative structures of *a*-Ta₂O_x generated along with their corresponding RDFs (see computational details in previous section). An O-O signal that is merely a shoulder for *a*Ta80O80 evolves into a well-defined peak near 2.7 Å as O content increases. Comparison of all the panels in Fig. 2.2 shows that *a*-Ta has a longer range order that disintegrates as the O content is increased. A gradual evolution in RDFs as O content is increased, especially between Figs. 2.2(e) and (f), suggests that structures initially derived from *c*-Ta are equivalent to structures initially derived from *c*-Ta₂O₅ using our QMD procedure. For the stoichiometric oxide, *a*Ta48O120, structural order is effectively washed out beyond 4 Å in the RDF. This result appears characteristic of *a*-Ta₂O₅ as similar results are reported by Bassiri *et al.* [1] and Wu *et al.* [30]. Bassiri *et al.* [1] attribute the limited short-range order to Ta₂O₂ ring fragments that might typically form during sputter deposition processes.

2.2. Conductivity Calculations

2.2.1. Optical conductivity

All conductivity calculations herein apply the Kubo-Greenwood formulation [31-33] described in numerous first-principles studies [34-40] to calculate optical conductivity, $\sigma(\omega)$, from the complex, frequency-dependent dielectric function, $\varepsilon(\omega)$, as implemented in VASP (atomic units):

$$\sigma(\omega) = \frac{2\pi e^2 \hbar^2}{3m^2 \omega \Omega} \sum_{i,j=1}^n \sum_{\alpha=1}^3 [F(\epsilon_{i,\mathbf{k}}) - F(\epsilon_{j,\mathbf{k}})] \times |\langle \Psi_{j,\mathbf{k}} | \nabla_{\alpha} | \Psi_{i,\mathbf{k}} \rangle|^2 \delta(\epsilon_{j,\mathbf{k}} - \epsilon_{i,\mathbf{k}} - \hbar\omega) \quad (2.1)$$

$$\varepsilon(\omega) = \varepsilon_1(\omega) + i\varepsilon_2(\omega) \quad (2.2)$$

In Eq. 2.1, \hbar is the reduced Planck's constant, ω is frequency, e and m are the charge and mass of the electron, respectively, Ω is the supercell volume, n is the number of Kohn-Sham states, and α is an index over all independent spatial directions. $F(\epsilon_{i,k})$ is a Fermi weight and $\Psi_{i,k}$ is the wave function corresponding to eigenvalue $\epsilon_{i,k}$. In Eq. 2.2, ϵ_1 and ϵ_2 are the real and imaginary components of the dielectric function, respectively. Equation 2.3 provides the relationship between complex conductivity and the complex dielectric function:

$$\epsilon_1(\omega) + i\epsilon_2(\omega) = \frac{4\pi i}{\omega} [\sigma_1(\omega) + i\sigma_2(\omega)] \quad (2.3)$$

The real component of electrical conductivity, σ_1 , as reported in this work is simply related to the imaginary component of the dielectric function as show in Eqns. 2.4 and 2.5 in Gaussian/CGS and MKSA units [51], respectively,

$$\sigma_1(\omega) = \frac{\omega \epsilon_2}{4\pi} \quad (2.4)$$

$$\sigma_1(\omega) = \omega \epsilon_o \epsilon_2 = \frac{E}{\hbar} \epsilon_o \epsilon_2, \quad (2.5)$$

where E is energy and ϵ_0 is the permittivity of free space.

DFT conditions for conductivity calculations were optimized separately for structures derived from *c*-Ta and *c*-Ta₂O₅ structures. In all cases, 14 QMD configuration snapshots, unless noted otherwise, were used as inputs for a two-step procedure to individually calculate $\sigma(\omega)$ for each snapshot with PBE [44] functionals. In addition, all calculations used 400 eV planewave cutoff energies, Fermi-Dirac statistics for electronic level occupation, and electronic temperatures set to match ionic temperatures from QMD simulation. Ta derivative structures used 10 kpoints to sample the BZ, while Ta₂O₅ derivatives used a 14-kpoint sampling. The extreme cost of hybrid calculations permitted only Γ -point calculations with the HSE06 functional [45,46]. We found $\sigma(\omega)$ converged up to about 10 eV with 200 empty conduction bands, so a 200 conduction band minimum was employed for all $\sigma_o = \sigma(\omega=0)$ calculations. In the first step, the charge density distribution was obtained for each configuration. In the second step, $\epsilon(\omega)$ was calculated from the optimized charge density distribution. For all but the most conductive Ta₂O_x compositions, a third calculation was run to refine the $\epsilon(\omega)$ from step two with the hybrid HSE06 [45,46] functional to produce more accurate (larger) band gaps and consequently more accurate $\sigma(\omega)$ data. Hybrid calculations became increasingly expensive in the pure metallic limit and less accurate than PBE calculations.

2.2.2. Sampling and averaging

We sampled QMD configurations after 1.5 ps equilibration and subsequently at 0.5 ps intervals at each temperature studied to effectively capture the phonon influence on finite temperature conductivity. Using this method, a $\sigma(\omega)$ curve is obtained for each individual configuration. Except where noted, the three normal components ($\epsilon_{xx}(\omega)$, $\epsilon_{yy}(\omega)$, $\epsilon_{zz}(\omega)$) computed for the 2nd order tensor quantity, $\epsilon(\omega)$, are immediately averaged to produce one $\sigma(\omega)$ curve. To condense data into a format suitable for both fitting and tabulation, an average $\sigma(\omega)$ curve was generated

for the configuration set at each condition studied. For metallic systems, the statistical variation of σ is adequately accommodated on a linear scale and follows a Gaussian distribution, so an arithmetic average to represent the population is appropriate. For insulating systems, the general expectation for statistical variation of σ changes to a logarithmic scale and follows a lognormal distribution [52], so a geometric or log average provides the best single statistic to represent the population. Exact treatment of conductivity distributions is an active research area where the details of system disorder, symmetry, dimensionality, and AC excitation ($\omega > 0$) all influence the actual distribution [53,54]. The equivalence of the geometric mean and log average (base 10) are shown in Eq. 2.6,

$$\left[\prod_{i=1}^n \sigma_i \right]^{1/n} = 10^{\left[\frac{1}{n} \sum_{i=1}^n \log_{10} \sigma_i \right]}, \quad (2.6)$$

where n is the population size. In practice, we found the log average more practical to compute for large populations ($n \geq 100$). In Section 7, we will justify our application of these statistics with a statistical analysis of conductivity.

2.2.3. DC extrapolation and fitting

As previously noted [34-36], the general method to calculate DC conductivity from $\sigma(\omega)$ data is to calculate $\sigma_0 = \lim_{\omega \rightarrow 0} \sigma(\omega)$. $\sigma(\omega)$ data unphysically falling toward zero represent numerical simulation artifacts that are a consequence of finite spacing in the eigenvalues that result from simulating finite-sized supercells, so this data is excluded prior to extrapolation. For derivatives of c -Ta, we fit $\sigma(\omega)$ to a Drude-model as described in numerous works on metallic systems [34-36],

$$\sigma(\omega) = \frac{\sigma_0}{(1 + \omega^2 \tau^2)}, \quad (2.7)$$

where τ is the free carrier lifetime. However, the added complexity of variable composition and even just amorphization of c -Ta (a -Ta) quickly produced $\sigma(\omega)$ data deviating from Drude-like behavior.

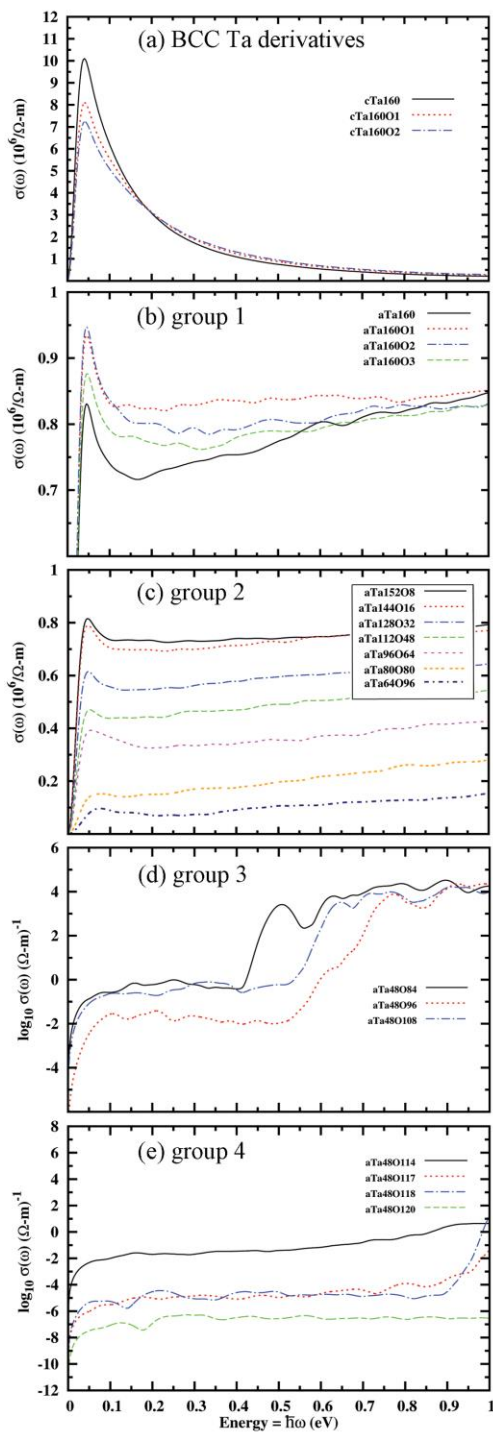


Figure 2.3. Diversity of 300K optical conductivity responses up to 1 eV as a function of composition in the Ta_2O_x ($0 \leq x \leq 5$, neutral V_O) system. (a)-(c) $\sigma(\omega)$ curves calculated with PBE functionals represent the arithmetic average over 12-14 MD configuration snapshots. (d)-(e) $\sigma(\omega)$ curves calculated with HSE06 functionals represent log averages over at least 6 MD configuration snapshots.

The fitting strategy applied is closely related to the categorization of structures presented in Section 2.1. Tables 2.1 and 2.2 collectively group the structures in this work into six categories that correspond to six fitting strategies. Appreciation of the fitting complexity across the Ta_2O_x spectrum is best conveyed in the $\sigma(\omega)$ response diversity displayed in Fig. 2.3. For the group 1 structures in Table 2.1, Drude-like behavior is confined to a narrow range between the first local maxima and first local minima; hence, fitting to the Drude function in Eq. 2.7 is applied only on this range. For the group 2 structures, $\sigma(\omega)$ data calculated with PBE functionals was generally fit with the same method as the group 1 structures, but $\sigma(\omega)$ calculated with HSE06 functionals instead applied a linear regression (linear $\sigma(\omega)$ scale) because the characteristic Drude maximum in the DC limit all but disappears with the HSE06 functional as O content increases. For group 3 and 4 structures, the fitting methods applied were essentially the same. These compositions exhibited sufficiently low σ to justify a log average representation of each $\sigma(\omega)$ curve. For group 3 and 4 structures, linear regressions were performed on semilog plots ($\log_{10}\sigma(\omega)$ scale) with a manually-determined energy range for PBE calculations, while linear regressions on semilog plots ($\log_{10}\sigma(\omega)$ scale) were used for HSE06 calculations over the energy range between the first local maxima and typically ~ 1 eV. The fitting procedure for σ_0 extrapolation from *c*- Ta_2O_5 structures was identical to that of the amorphous group 4 structures, except for the explicit treatment of the three spatial components of DC conductivity ($\sigma_{0,xx}$, $\sigma_{0,yy}$, and $\sigma_{0,zz}$).

3. EXPERIMENTAL METHODS

Ceramic Ta₂O₅ pellets were formed by mixing commercial Ta₂O₅ powder (H.C. Starck, 99.9%) with 0.5 wt.% polypropylene carbonate-based binder (QPAC40, Empower Materials) in aqueous emulsion, drying at 120 °C overnight, then consolidating the powders in a 12.7mm diameter die under ~85 MPa uniaxial pressure. The resulting ~2mm thick disks were then further compacted under 150 MPa of hydrostatic pressure. These pellets were sintered in a tube furnace in Al₂O₃ crucibles at 1320 °C for 12 hours with a ±5 °C/min ramp rate under either static air or flowing O₂ gas. The resulting pellets were >99% dense as measured using a standard fluid displacement technique. The surfaces of the pellets were then ground to a 1µm finish and 200 nm thick Au electrodes were sputter deposited on each face over a 20 nm thick Cr adhesion layer.

Ta₂O₅ pellet resistance was measured using a Keithley 237 high voltage source measure unit with a shielded connection to a custom-fabricated low-noise sample holder inserted in a laboratory environmental chamber (Sun Electronic Systems, Inc.). A constant 400V bias was maintained across the pellet while current measurements were collected approximately twice per second using a custom LabView interface while the environmental chamber ramped to 300 °C and back down to ambient temperature with a ±5 °C/min ramp rate. Temperature was monitored simultaneously with an HP3478 digital multimeter attached to a K-type thermocouple with cold junction compensation.

Ta₂O_x thin films were sputter-deposited from a 323 mm diameter Ta sputter target with a power density of 1.25 W/cm² (1kW DC pulsed at 100 kHz) and a sample-target distance of ~100 mm in a base chamber pressure of 2×10⁻⁸ torr. The sputter pressure was maintained at 5.5 mtorr, while the O stoichiometry was simultaneously controlled by adjusting the Ar:O₂ ratio of sputter gas mixture between ratios of 100:0 and 155:44. Films for this study were deposited on sections of Si wafers with 100 nm of thermal oxide (thickness ranged from 57.9 to 154 nm as measured by a contact profilometer (Dektak 6M)). The Ta:O ratio was characterized in our samples via both Rutherford backscattering (RBS) and X-ray photoelectron spectroscopy (XPS) techniques.

Thin film resistance measurements were performed using a linear 4-point probe with spring-loaded tungsten carbide contacts spaced 1 mm apart using a Keithley 236 Source Measure Unit as the current source and a Keithley 181 nanovoltmeter as the voltage probe. Care was taken to maintain voltages << 1 mV in order to minimize any nonlinear or hysteretic effects in the Ta₂O_x films.

This page intentionally left blank.

4. CRYSTALLINE MONOVACANCY STABILITY

We verified the structure and energetics of the O monovacancy in three charge states (V_O^n ; $n=0,1+,2+$) in the 168-atom expansion of the Ramprasad model for c - Ta_2O_5 as the simplest defect in the Ta_2O_x system. Figure 4.1 depicts the structure of each V_O^n relative to bulk c - Ta_2O_5 , while Fig. 4.2 shows the distribution of total energies obtained for each charge state. We adopted the nomenclature of Ramprasad [2,3] in categorizing the O sites loosely into four groups as illustrated in Fig. 2.1(c). Since the c - Ta_2O_5 structure is layered, O sites are only differentiated by their location in the z plane.

Only total energy differences (E_{rel}^n) are provided in Fig. 4.2 because we felt the lack of a well-defined reference crystal imparts systematic, yet indeterminate, uncertainty into conventional formation energy calculations. In addition, our goal in studying the monovacancy structure was mainly to ascertain minimum energy structures from a small statistical sample set for each charge state as input structures for conductivity and other property calculations. For each charge state, at least five independent configurations (six for site 4) representing each of four O site categories for a total of 21 configurations was sampled. Structures were relaxed and accurate total energy calculations were made as described in Section 2. For V_O^0 , a site 4 equatorial configuration emerged as the minimum energy configuration. From the E_{rel}^0 distribution, V_O^0 is clearly stabilized in equatorial sites (sites 3 and 4), while the cap sites (site 1 and 2) are consistently less stable configurations. Ramprasad [3] also identified site 4 as the ground state configuration for V_O^0 . For both V_O^{1+} and V_O^{2+} , the cap site configuration of site 1 emerged as the minimum energy configuration. Contrary to the neutral case, the E_{rel}^{1+} and E_{rel}^{2+} distributions suggest both cap sites stabilize positively charged O vacancies, with the TaO_7 cap site being most favorable. While Ramprasad [3] found site 4 preferred for V_O^{2+} , the difference in conclusions is likely a result of our increased statistical sampling. Note that we found a site 4 configuration for V_O^{2+} to be the fourth lowest energy configuration in our population.

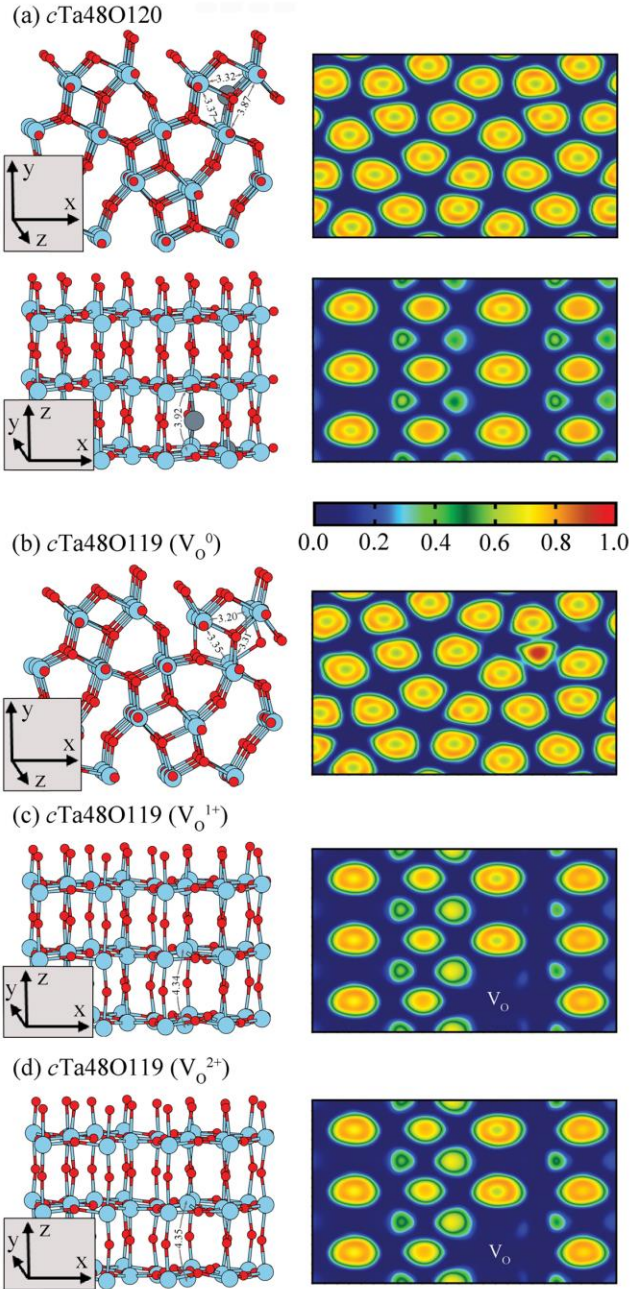


Figure 4.1. Configurations of bulk $c\text{-Ta}_2\text{O}_5$ and the monovacancy in various charge states (left) with corresponding ELF contours (right). Tantalum and oxygen atoms are represented by light blue and red spheres, respectively, while dark grey spheres in (a) indicate O lattice sites for V_{O} creation. Provided measurements (\AA) indicate separation of neighboring Ta atoms near V_{O} sites. Qualitative interpretation of ELF values: 1.0 represents perfect localization, 0.5 represents metallic regions of free electron gas, and 0.0 represents regions of zero electron density. Coordinate axes apply to both structural configurations and ELF contour plots; however, the view axis that is skewed off-axis for structure depth perspective is parallel to the reader's view in the ELF contours.

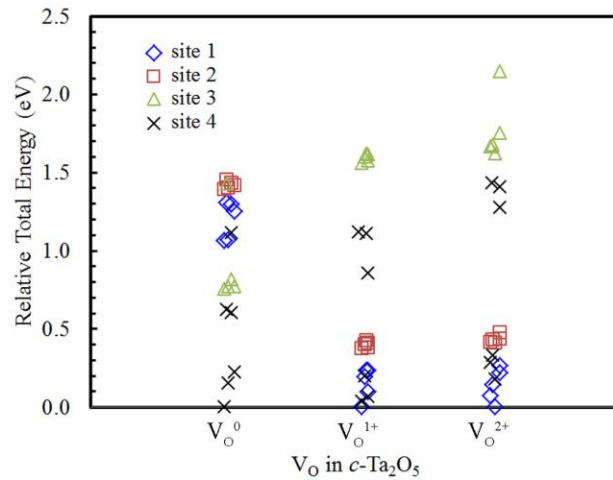


Figure 4.2. Total energy distributions of the c -Ta₂O₅ monovacancy in three charge states in 168-atom supercells. Jitter was added to the horizontal access for visual clarity. For each charge state, a minimum of 5 configurations were sampled from each O site category (21 total configurations). The lowest energy for each charge state is the representative configuration used for property calculations.

The three minimum energy configurations (V_O^0 , V_O^{1+} , and V_O^{2+}) are illustrated in Figs. 4.1(b)-(d). For V_O^0 , the surrounding lattice, especially in-plane, tends to contract in toward the vacancy relative to c -Ta₂O₅ in Fig. 4.1(a). In contrast, the presence of either V_O^{1+} or V_O^{2+} in a cap site configuration strongly repels the Ta NNs apart. In Fig. 4.1, the separation distance of NN Ta atoms swells by over 0.4 Å around the positively-charged O vacancies. The charge-dependent expansion/contraction of the lattice surrounding a V_O was similarly reported in recent first-principles studies in aluminum oxide [12,13].

This page intentionally left blank.

5. ELECTRICAL CONDUCTIVITY

Tables 2.1 and 2.2 provide a summary of our electrical conductivity calculations at three different temperatures with two different functionals for a variety of different Ta_2O_x compositions in both amorphous and crystalline phases, respectively. Overall, expected trends of decreasing σ_0 with increasing O content and increasing σ_0 with increasing temperature are reproduced in our first-principles conductivity data. In general, sampling only a single representative amorphous structure at most compositions is likely the main contributor to noise in the property trends. The significance of sampling a set of independently-quenched amorphous structures for property determination will be explored in Section 7. The optical conductivities at 300K associated with the summarized σ_0 data in Tables 2.1 and 2.2 are contained in Fig. 2.3.

Our σ_0 data at 300K from Table 2.1 is correlated with our ambient temperature conductivity measurements on experimentally grown Ta_2O_x thin films and bulk Ta_2O_5 pellets in Fig. 5.1.

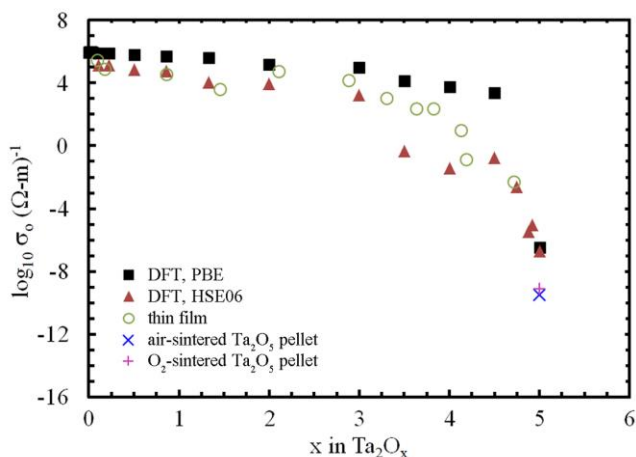


Figure 5.1. Correlation of DC conductivities at 300K for α - Ta_2O_x ($0 \leq x \leq 5$, neutral V_O) calculated from DFT calculations (solid shapes) for both PBE and HSE06 functionals with experimental conductivity measurements (open shapes) on both Ta_2O_x ($0.18 \leq x \leq 4.72$) thin films and air- and O_2 -sintered bulk Ta_2O_5 pellets. DFT σ_0 values are those represented in Table 2.1.

The hybrid HSE06 σ_0 values are consistently lower than our PBE σ_0 values at all values of x , which largely corresponds to the consistently larger and more accurate E_g from the hybrid calculations. This functional dependence is consistent with the σ_0 calculations of French *et al.* [40] in water under warm dense matter conditions. The difference in σ_0 from PBE and HSE06 calculations widens as the E_g increases at larger values of x . Our DFT predictions show generally good agreement with experiment. Both DFT and experimental results exhibit a knee in the σ_0 vs. composition dependence in which σ_0 varies much more rapidly for $x \geq 4$ to 4.5. The DFT σ_0 results are more consistent with experiment in the metallic limit, while thin film σ_0 ($2.0 \leq x \leq 4.75$) measurements are generally intermediate to the PBE and HSE06 σ_0 results. As anticipated, the DFT results have more variability and are harder to match to experiment on the insulating end of the composition spectrum. For select compositions, additional independent

structures were generated for better statistical sampling and resulted in better clarification of the DFT σ_0 trend. The statistical contribution to DC conductivity will be explored further in Section 7. The lowest conductivities obtained were 6.94×10^{-10} and $3.01 \times 10^{-10} (\Omega\text{-m})^{-1}$ from the O_2 - and air-sintered Ta_2O_5 pellets, respectively. The slightly higher σ_0 value for the O_2 -sintered pellet compared to the air-sintered pellet is contrary to expectation and suggests the possibility of unintentional acceptor dopant (likely metallic impurities) atoms present. The Ta_2O_5 pellet values are nearly 3 orders of magnitude lower than the lowest σ_0 obtained from DFT simulation. The artificial conductivity floor observed for insulating $a\text{-Ta}_2\text{O}_x$ compositions with DFT calculations is at least in part a consequence of partially converged calculations with respect to supercell size. Supercells as large as 672 atoms for $a\text{-Ta}_2\text{O}_5$ were checked without observing full convergence, so complete convergence with respect to supercell size is impractical.

In addition to our own conductivity measurements, a limited number of publications concentrating on the endpoint compositions provide additional basis for comparison. We calculated $1.1 \times 10^7 (\Omega\text{-m})^{-1}$ for σ_0 of BCC Ta at 300K in a 160-atom supercell, while the tabulated value in Ref. 47 is $7.4 \times 10^6 (\Omega\text{-m})^{-1}$. The DFT calculation is a 45% overestimate for 160 atoms, but shrinks to a 5% underestimation with a 432-atom supercell. For $a\text{-Ta}$ σ_0 , we calculated $8.7 \times 10^5 (\Omega\text{-m})^{-1}$, while Nestell *et al.* [17] reported $4.4 \times 10^5 (\Omega\text{-m})^{-1}$ for their amorphous films. Sputtered Ta thin films with significant BCC crystallization morphology can exhibit σ_0 values as high as 2 to $5 \times 10^6 (\Omega\text{-m})^{-1}$ [16]. Baker [16] reports a range of 1×10^4 to $1 \times 10^6 (\Omega\text{-m})^{-1}$ for Ta thin films with dissolved O. Similarly, we have a spread of $2 \times 10^3 (\Omega\text{-m})^{-1}$ ($a\text{Ta}64\text{O}96$, HSE06) up to $8 \times 10^5 (\Omega\text{-m})^{-1}$ ($a\text{Ta}152\text{O}8$, PBE) in our group 2 amorphous samples. Gnanarajan *et al.* [21] reports σ_0 values of 3 to $4 \times 10^5 (\Omega\text{-m})^{-1}$ for Ta_2O (33% O), while our $a\text{Ta}112\text{O}48$ (30% O) similarly has a range of 6×10^4 to $5 \times 10^5 (\Omega\text{-m})^{-1}$ from the two functionals. Baker also reports a range of 1×10^{-5} to $1 \times 10^{-7} (\Omega\text{-m})^{-1}$ for Ta_2O_5 thin films, while we found $2 \times 10^{-7} (\Omega\text{-m})^{-1}$ for $a\text{Ta}48\text{O}120$ with the HSE06 functional. Ta_2O_5 σ_0 values in the literature can be extracted from various studies of dielectric breakdown; as a result, reported values cover a wide range (1×10^{-5} to $1 \times 10^{-11} (\Omega\text{-m})^{-1}$) and are influenced by extreme current densities and electric field magnitudes, as well as the inherent quality of the deposited films [18,19,55]. The largest sources of error in our DFT calculations originate in the small supercell sizes used and are manifested in discretization of eigenvalues and inadequate sampling of ideally random networks in the amorphous structures. Overall, experimental measurements, especially on amorphous thin films, are often clouded by accurate characterization of the sample material because factors including deposition technique, annealing procedure, film homogeneity, measurement technique, impurity incorporation, film density, and surface roughness all potentially influence reported conductivities.

5.1. Metallic Ta

The low frequency optical conductivity responses for crystalline and amorphous Ta as a function of temperature are provided in Fig. 5.2. Amorphization of Ta alone is responsible for an order of magnitude reduction in σ_0 . The Drude function (Eq. 2.7) decreases monotonically as ω increases. Aside from the discretization simulation artifact near $\omega=0$, this Drude behavior is exhibited in the crystal phase, but a departure from Drude behavior is observed a couple tenths of an eV above the $\sigma(\omega)$ maximum in the amorphous case in which $\sigma(\omega)$ remains flat or even

increases. This intermediate frequency behavior in $\sigma(\omega)$ is also reported by Nestell *et al.* [17]. Perhaps more importantly, the temperature dependence of conductivity or thermal coefficient of resistivity (TCR) changes sign for Ta merely from amorphization. For the crystalline case, σ_0 decreases as temperature increases, characteristic of a metal; however, σ_0 increases as temperature increases in the amorphous case, which is an insulator characteristic. This is an unexpected result since we expected to observe a metal-insulator-transition (MIT) at some intermediate composition of a -Ta₂O_x.

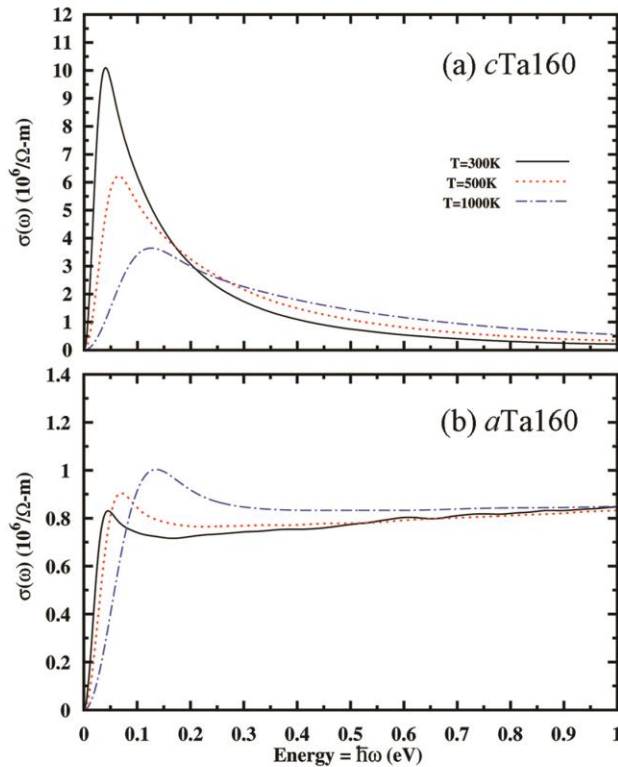


Figure 5.2. Optical conductivities contrasting the temperature dependence by phase in 160-atom supercells of (a) BCC Ta and (b) amorphous Ta. All $\sigma(\omega)$ curves represent the arithmetic average over 14 MD configuration snapshots. Spatial components $\sigma_{xx}(\omega)$, $\sigma_{yy}(\omega)$, $\sigma_{zz}(\omega)$ are identical through BCC symmetry and therefore averaged.

5.2. Amorphous Ta₂O_x

Figure 5.3 provides the optical conductivity responses of near-stoichiometric compositions of a -Ta₂O_x in various charge states as a function of temperature. Comparison of Figs. 5.3(a) and (b) reveals the effect of the two functionals on $\sigma(\omega)$ seen throughout this work. In both cases, a step occurs in conductivity at the E_g energy; however, the benefit of using the HSE06 functional is seen in the larger, more accurate E_g . At the low temperature reference of 10 K, E_g is only about 3 eV for a Ta₄₈O₁₂₀ with the PBE functional, while E_g is nearly 4.5 eV with the HSE06 functional. Experimentally reported values for the Ta₂O₅ E_g range from 3.9 to 5.28 eV [18,19], but the average value is about 4 eV; this wide range is typical of many dielectrics and is a result of the variability in dielectric quality and sometimes band gap definition. As temperature increases, the E_g for both functionals decreases and the corresponding step function in $\sigma(\omega)$

softens. Interestingly, $\sigma(\omega)$ at 10K in Fig. 5.3(b) is both noisier and not bound by the artificial conductivity floor that is evident around $1 \times 10^{-8} (\Omega\text{-m})^{-1}$ in Fig. 5.3(a) and is attributable to the use of finite supercells. In addition, the choice of functional has some effect on the temperature dependence of σ . It is evident that many σ_0 values for the HSE06 functional in Fig. 5.3(b) are approximately three orders of magnitude lower than those from the PBE functional in Fig 5.3(a).

The insertion of a single, neutral oxygen vacancy (V_O^0) has a strong effect on the optical conductivity as illustrated in Fig. 5.3(c) for $a\text{Ta}_48\text{O}_{119}$. V_O^0 presence notably influences the temperature dependence of $\sigma(\omega)$ and is indicative of the often cited [12,13,56] dopant-like behavior of O vacancies in most MO_x materials. The presence of V_O^0 appears to sharpen the temperature dependence of $\sigma(\omega)$ as observed over 30 decades of conductivity. At cryogenic temperatures, no finite σ_0 is observed in simulation, while σ_0 surges to $1 \times 10^4 (\Omega\text{-m})^{-1}$ at 1200K. While no finite σ_0 is observed at cryogenic temperatures, a trend for decreasing threshold ω required for the onset of finite σ is seen as temperature increases. The onset of finite σ_0 occurs between 300 and 400K in our simulation results and σ_0 rises another 16 orders of magnitude between 400 and 500K. Our results suggest that modulation of σ_0 in Ta_2O_5 is possible through control of both V_O^0 concentrations near 1% and temperatures just above ambient.

Examination of Figs. 5.3(d) and (e) emphasize the influence of V_O charge state on conductivity. For V_O^{1+} , there is little temperature dependence seen, except at the 10K reference, and V_O^{1+} appears weakly metallic with $\sim 1 \times 10^4 (\Omega\text{-m})^{-1}$ σ_0 at most temperatures up through 1200K. Further oxidation from V_O^{1+} to V_O^{2+} results in a family of $\sigma(\omega)$ curves that is essentially indistinguishable from those of the bulk oxide in Fig. 5.3(b). As a result, the V_O charge state appears crucial to conductivity in near-stoichiometric $a\text{-Ta}_2\text{O}_x$.

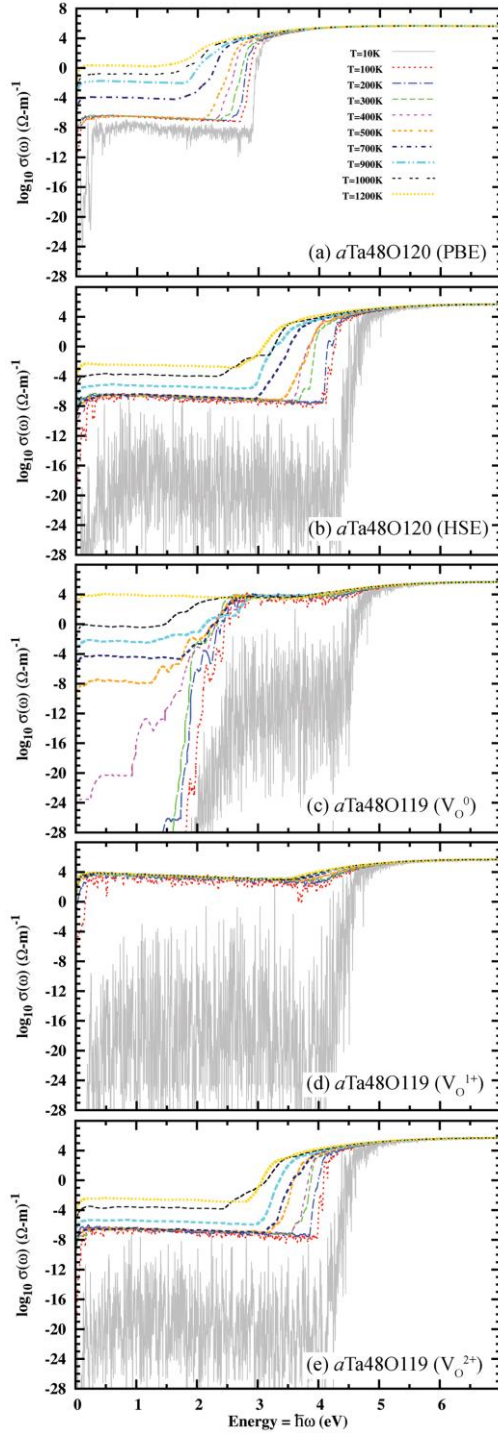


Figure 5.3. Optical conductivity curves at 10 temperatures in near-stoichiometric compositions of a - Ta_2O_x in 168-atom basis supercells. $\sigma(\omega)$ for a - Ta_2O_5 calculated with (a) PBE and (b) HSE06 functionals. $\sigma(\omega)$ calculated with HSE06 functionals for (c) V_O^0 , (d) V_O^{1+} , and (e) V_O^{2+} in a - Ta_2O_5 . $\sigma(\omega)$ curves calculated with PBE functionals represent the arithmetic average over a minimum 14 MD configuration snapshots, while $\sigma(\omega)$ curves calculated with HSE06 functionals represent the log average over a minimum 6 MD configuration snapshots.

In Fig. 5.4, the dopant-like behavior and sensitivity to V_O charge state is generalized for the insertion of additional O vacancies. The presence of two neutral V_O in $aTa48O118$ (1.7% V_O) is sufficient to produce finite σ_0 at 300K, while full oxidation of both O vacancies to V_O^{2+} again results in an $\sigma(\omega)$ response indistinguishable from bulk $aTa48O120$. Similarly, the presence of three neutral V_O in $aTa48O117$ (2.5% V_O) results in finite σ_0 , but complete oxidation to three V_O^{2+} again quenches the $\sigma(\omega)$ back to that of stoichiometric $aTa48O120$.

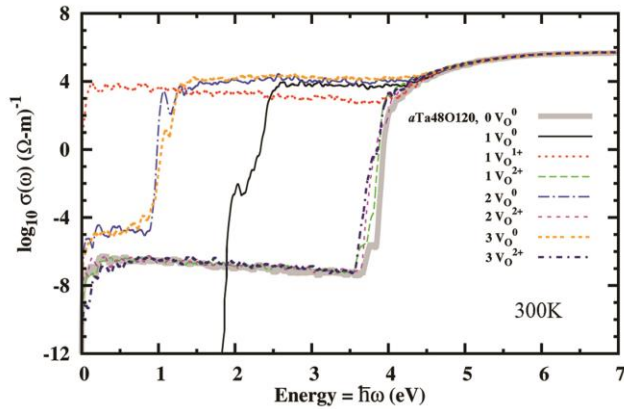


Figure 5.4. Optical conductivities at 300K for near-stoichiometric compositions of a - Ta_2O_5 with V_O^n in various charge states ($n = 0, 1+, 2+$). The thick grey line references $\sigma(\omega)$ for stoichiometric a - Ta_2O_5 . All $\sigma(\omega)$ curves represent the log average over a minimum 6 MD configuration snapshots.

5.3. Crystalline Ta_2O_x

The dopant-like behavior observed in Fig. 5.3 on a - Ta_2O_x structures is further generalized for c - Ta_2O_x in Fig. 5.5. While Fig. 5.5 only shows the temperature dependence of conductivity for $\sigma_{zz}(\omega)$, the simulation results were largely similar in the other principle directions. One difference seen in the crystalline case is a subdued temperature dependence for $\sigma_{zz}(\omega)$. In particular, finite σ_0 was observed for V_O^0 at 300K and σ_0 at 400K is much higher at $1 \times 10^{-9} (\Omega\text{-m})^{-1}$. The increase in σ_0 from 400 to 500K is only about 3 decades for V_O^0 in c - Ta_2O_x compared to 16 decades for a - Ta_2O_x . At high temperatures, σ_0 at 1200K is lower for V_O^0 in c - Ta_2O_x at $1 (\Omega\text{-m})^{-1}$, rather than $1 \times 10^4 (\Omega\text{-m})^{-1}$ for a - Ta_2O_x . The modulation of σ by the charge state of V_O is similar for the crystalline case as observed in Fig. 5.3. V_O^{1+} in $cTa48O119$ again looks like a weakly conductive metal with little temperature dependence, while V_O^{2+} in $cTa48O119$ exhibits a family of $\sigma_{zz}(\omega)$ curves that are nearly the same as the bulk $cTa48O120$ case.

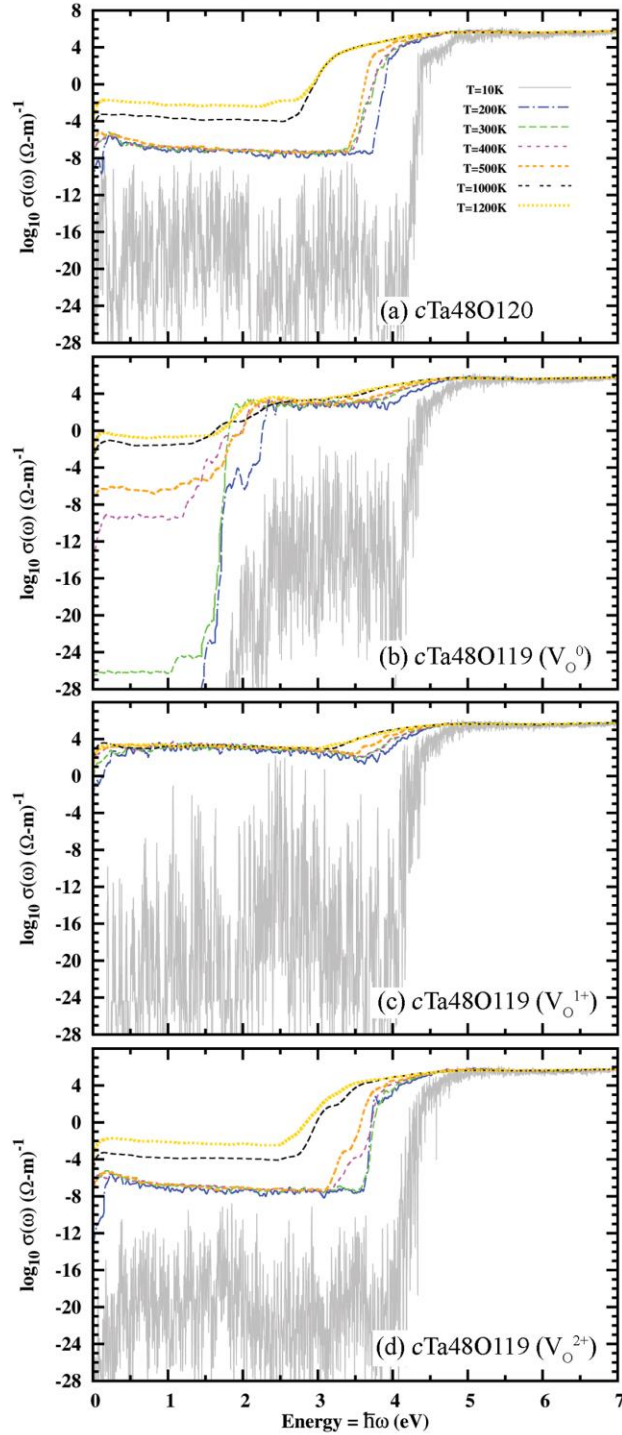


Figure 5.5. Optical conductivity curves at seven temperatures in near-stoichiometric compositions of $c\text{-Ta}_2\text{O}_x$ in 168-atom basis supercells. $\sigma(\omega)$ are shown only for zz normal components ($\sigma_{zz}(\omega)$) calculated with HSE06 functionals for (a) bulk $c\text{-Ta}_2\text{O}_5$, (b) V_O^0 , (c) V_O^{1+} , and (d) V_O^{2+} . All $\sigma(\omega)$ curves represent the log average over a minimum 6 MD configuration snapshots.

Figure 5.6 provides a qualitative comparison of the anisotropy in conductivity exhibited by bulk c -Ta₂O₅. The dependence of $\sigma(\omega)$ on direction in c -Ta₂O₅ is much less than anticipated, possibly because the irregularities and distortion in the symmetries and crystal structure previously described in the Ramprasad simplification of the SR model muddle the differences among principle directions. In addition, the large unit cell of the SR model tends to average out spatial differences and produce more isotropic properties than most crystals. From Fig. 5.6, it is not surprising that slightly more anisotropy is observed at lower temperatures. $\sigma_{zz}(\omega)$ also shows a bump in conductivity in the DC limit not apparent in either $\sigma_{yy}(\omega)$ or $\sigma_{xx}(\omega)$. This signature is also generally seen in the $\sigma_{zz}(\omega)$ responses in Fig. 5.5. Some distinction for $\sigma_{zz}(\omega)$ from the other principle directions is consistent with the layered structure of the Ramprasad c -Ta₂O₅ model.

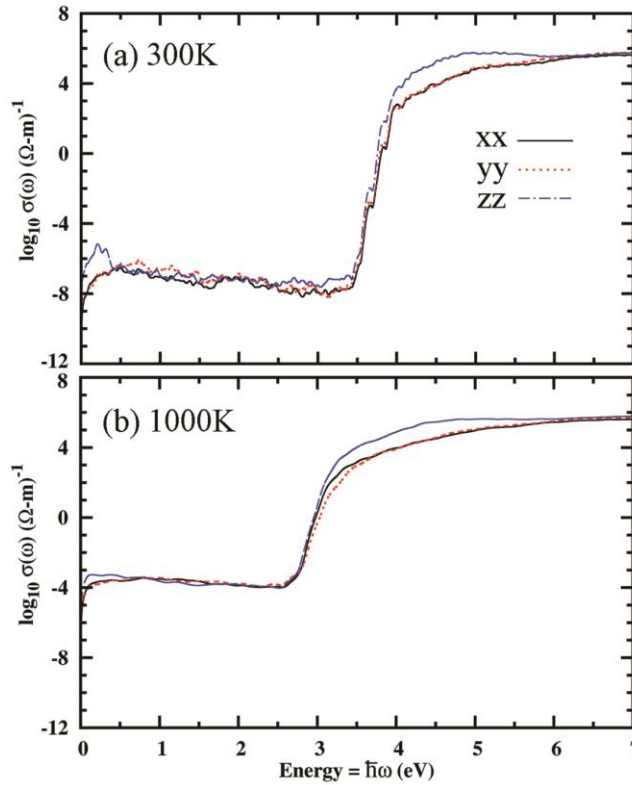


Figure 5.6. Optical conductivities for three normal components in bulk c -Ta₂O₅ calculated with HSE06 functionals at (a) 300K and (b) 1000K. All $\sigma(\omega)$ curves represent the log average over a minimum 6 MD configuration snapshots.

5.4. Amorphous TiO_x

Similar to Fig. 5.4, Fig. 5.7 shows that the dopant-like behavior and sensitivity to V_O^n charge state is also observed in a -TiO_x and may be a general character of O vacancies in TMO materials. In the 216-atom basis supercells used for a -TiO_x, the single monovacancy corresponds to a V_O concentration of 0.7%. Since a qualitative trend for increasing σ_0 is not seen in a -TiO_x as V_O^0 concentration increases, the nearly saturated σ_0 trend may suggest that $\sim 1\%$ V_O in a -TiO_x is a relatively higher dopant concentration than similar dopant levels in a -Ta₂O_x. Most

importantly, the signature of complete oxidation of all V_O^0 to V_O^{2+} in $a\text{-TiO}_x$ effectively quenching the $\sigma(\omega)$ back to that of stoichiometric $a\text{Ti}_72\text{O}_{144}$ is evident.

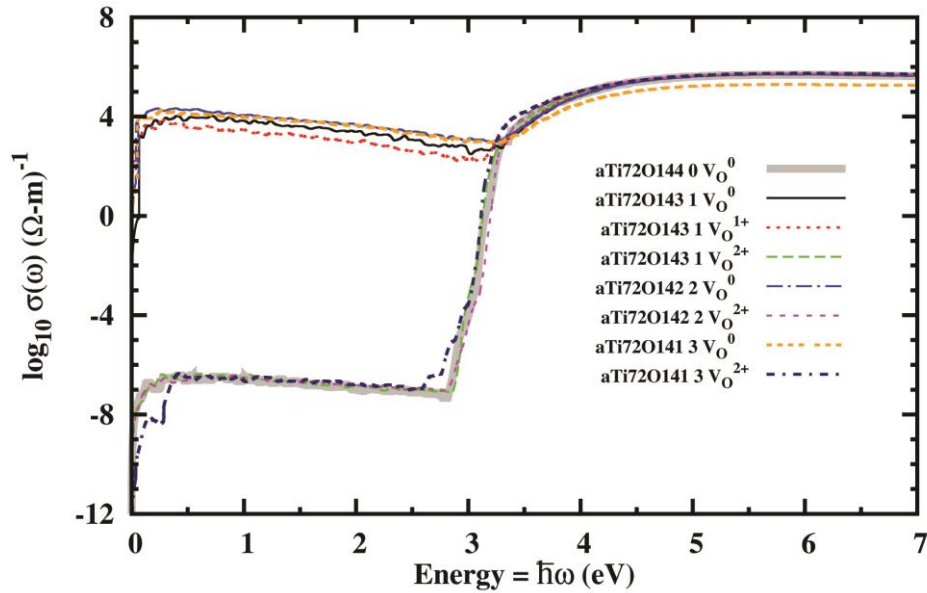


Figure 5.7. Optical conductivities at 300K for near-stoichiometric compositions of $a\text{-TiO}_2$ with V_O^n in various charge states ($n = 0, 1+, 2+$). The thick grey line references $\sigma(\omega)$ for stoichiometric $a\text{-TiO}_2$. All $\sigma(\omega)$ curves represent the log average over 10 to 14 MD configuration snapshots.

The temperature-dependent optical conductivity data presented in Fig. 5.8 is analogous to that presented in Fig. 5.3 for $a\text{-Ta}_2\text{O}_x$. The sharp step in $\sigma(\omega)$ observed near 3.5 eV at 10K in all structures corresponds to the E_g of TiO_2 and is fairly well-represented by the HSE06 functional. As seen in $a\text{-Ta}_2\text{O}_x$, the temperature dependence of $\sigma(\omega)$ is essentially the same for the $a\text{Ti}_72\text{O}_{144}$ and $a\text{Ti}_72\text{O}_{143}$ (V_O^{2+}) cases in Figs. 5.8(a) and (c), respectively. Again, the presence of V_O^0 in $a\text{-TiO}_2$ sharpens the overall temperature dependence of $\sigma(\omega)$ as shown in Fig. 5.8(b). Notably different for $a\text{-TiO}_2$ is the apparent minimum threshold for finite σ_0 . Additional temperatures were sampled at 30, 50, and 70K for the V_O^0 case in Fig. 5.8(b) to illuminate rapid σ changes at cryogenic temperatures. The additional data reveals the onset of finite σ_0 occurring between 30 and 50K for V_O^0 in $a\text{Ti}_72\text{O}_{143}$. Between 50 and 70 K, σ_0 increases approximately 20 orders of magnitude from $\sim 1 \times 10^{-27}$ to $\sim 1 \times 10^{-7} (\Omega\text{-m})^{-1}$. For 300K and higher temperatures, the σ_0 for V_O^0 in $a\text{Ti}_72\text{O}_{143}$ quickly saturates to weakly metallic behavior at $\sim 1 \times 10^4 (\Omega\text{-m})^{-1}$.

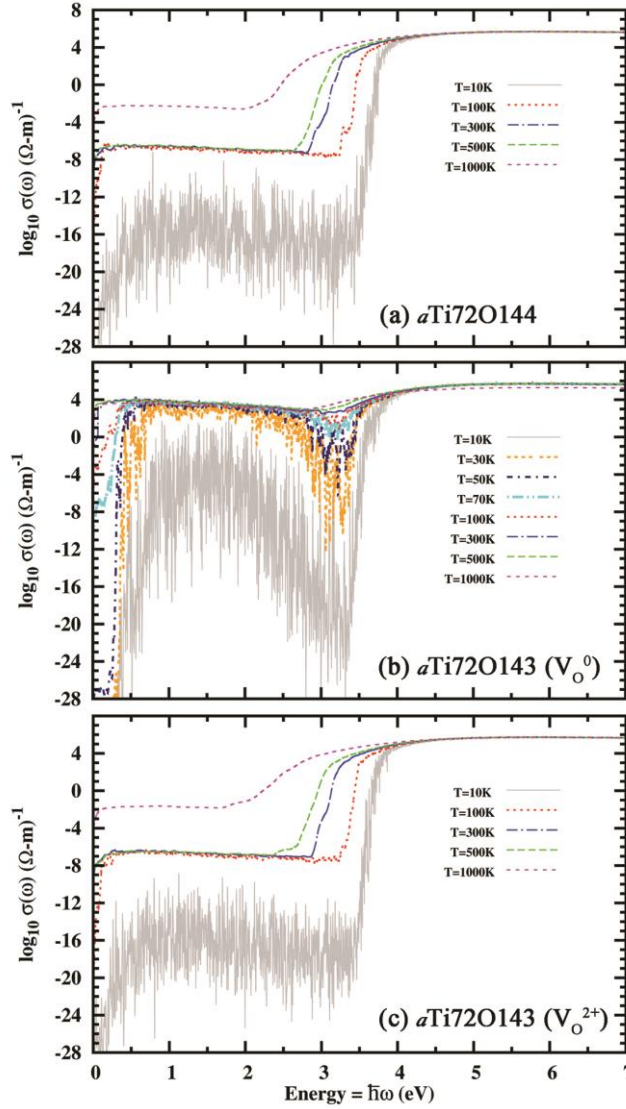


Figure 5.8. Optical conductivity curves at various temperatures in near-stoichiometric compositions of a - TiO_x in 216-atom basis supercells. $\sigma(\omega)$ calculated with HSE06 functionals for (a) a - TiO_2 , (b) V_O^0 in a - TiO_2 , and (c) V_O^{2+} in a - TiO_2 . All $\sigma(\omega)$ curves represent the log average over 10 to 14 MD configuration snapshots.

6. ELECTRONIC STRUCTURE

The underlying electronic structure ultimately determines the electronic conductivities we've presented in this work. In the following sections, we will strengthen conclusions made from conductivity results in O-deficient Ta₂O_x through additional investigation of electronic structure.

6.1. Band Gaps

Band gap data is presented for most Ta₂O_x compositions at 300K in Tables 2.1 and 2.2. A trend in E_g in group 4 in Table 2.1 is hard to discern because the changes in V_O concentration are small. A trend for decreasing E_g as V_O concentration increases is seen in group 3 and E_g quickly vanishes at the high V_O concentrations of group 2. In general, we find E_g for the amorphous phases to be slightly larger than equivalent compositions in the crystalline phase.

As previously discussed, step functions in the $\sigma(\omega)$ responses in Figs. 5.3 and 5.5 strongly correlate with E_g and the band gap is strongly correlated with temperature. This observation alone emphasizes the importance of using a hybrid functional or other corrective method for the DFT E_g in order to calculate accurate conductivities. Table 6.1 specifically quantifies the dependence of E_g on both phases and temperature in stoichiometric Ta₂O₅. The amorphous values are consistently higher than their crystalline counterparts at all temperatures. Band gap values at 1200K are roughly 1/3 of their values at 10K.

Table 6.1. Computed Ta₂O₅ band gaps as a function of temperature calculated with HSE06 functionals. Values represent averages over a minimum of 6 MD configuration snapshots with uncertainties provided as standard deviations.

	<i>c</i> Ta48O120	<i>a</i> Ta48O120
T (K)	E_g (eV)	E_g (eV)
10	4.2 ± 0.0	4.3 ± 0.0
200	3.6 ± 0.1	3.9 ± 0.1
300	3.3 ± 0.2	3.5 ± 0.1
400	3.2 ± 0.1	3.3 ± 0.1
500	3.0 ± 0.1	3.2 ± 0.2
700	2.4 ± 0.3	2.6 ± 0.2
1000	1.7 ± 0.2	1.8 ± 0.4
1200	1.4 ± 0.3	1.6 ± 0.2

6.2. Density of States

The density of states associated with single configurations of select *a*-Ta₂O_x compositions at 300K is provided in Fig. 6.1. In Fig. 6.1(a), the Fermi level lies about 0.5 eV above the valence band maximum (VBM). In Fig. 6.1(b), insertion of V_O⁰ creates a deep-level state with a high probability of occupation, so the Fermi level lies above the V_O⁰ defect state and below the conduction band minimum (CBM). This change in the electronic structure is qualitatively consistent with insertion of a typical donor dopant into a semiconductor. Oxidation of V_O⁰ to V_O¹⁺ in Fig. 6.1(c) moves the Fermi level into the bottom of the conduction band. This change in electronic structure is similar to the effect of degenerately doping a semiconductor with donor

atoms and is consistent with the conductivity values representative of weakly metallic conduction described in Section 5. The DOS for V_O^{2+} in Fig. 6.1(d) is nearly indistinguishable from the bulk α - Ta_2O_5 DOS, just as the $\sigma(\omega)$ responses in Figs. 5.3(b) and (e) are essentially indistinguishable. These results again suggest that full oxidation of V_O populations in O-deficient Ta_2O_5 effectively quenches electrical conductivity and reinforces the significance of the V_O charge state in conduction mechanisms. In Figs. 6.1(e)-(h), the insertion of additional V_O^0 into α - Ta_2O_5 is remarkably quantifiable through analysis of defect levels and magnitudes present in the gap. The insertion of additional V_O^0 eventually builds an intermediate band of defect levels while simultaneously moving the Fermi level closer to CBM. This observation is again consistent with the effect of increasing the concentration of a donor dopant in a semiconductor.

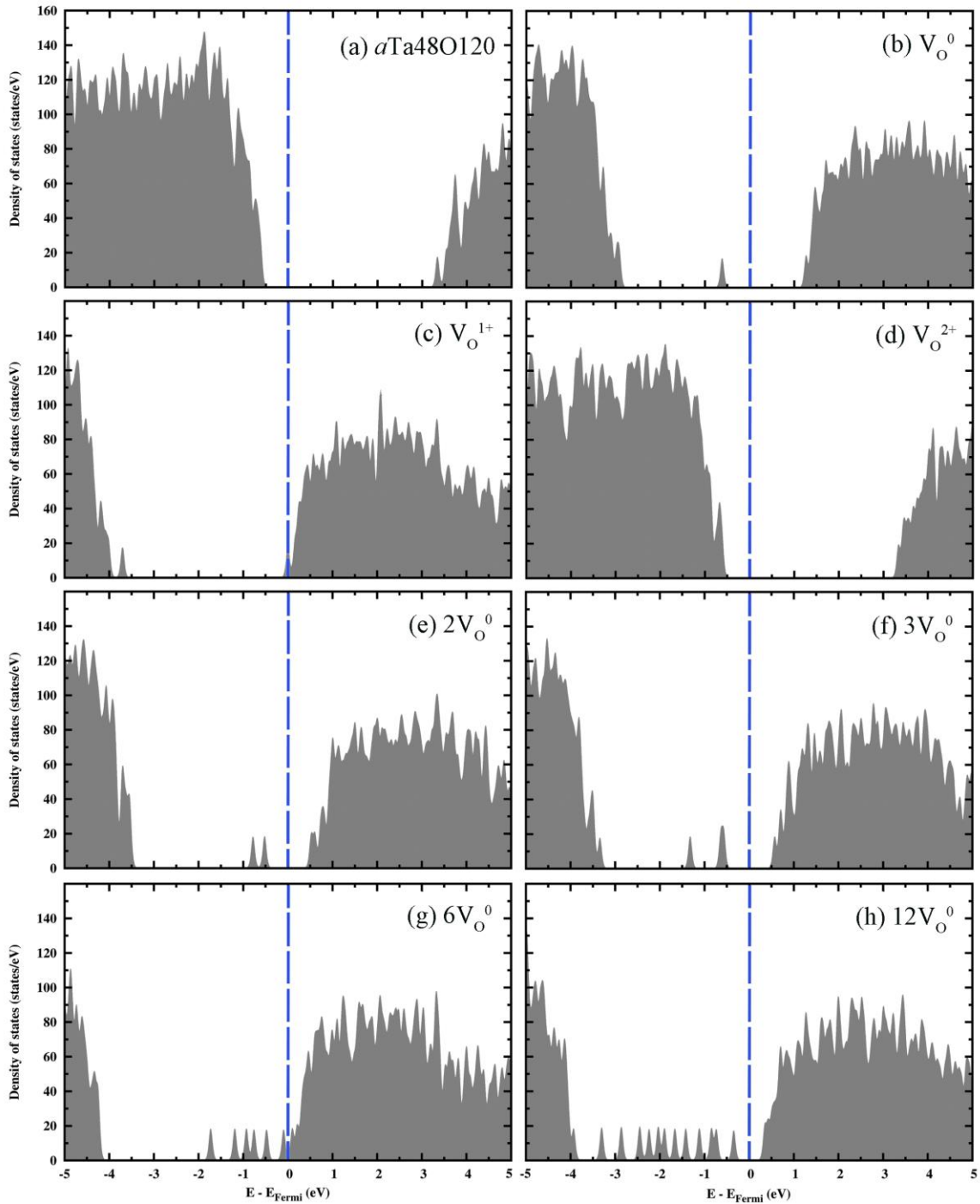


Figure 6.1. Total density of states for eight compositions of $a\text{-Ta}_2\text{O}_x$ where each figure represents one MD configuration snapshot at 300K. Vertical, dashed blue lines reference the Fermi level for each configuration. A reference TDOS is shown in (a) for $a\text{-Ta}_2\text{O}_5$, while the effect of the monovacancy in three charge states is shown in (b) V_O^0 , (c) V_O^{1+} , and (d) V_O^{2+} . The cumulative effect of additional neutral V_O on TDOS is shown in (e) 2V_O , (f) 3V_O , (g) 6V_O , and (h) 12V_O .

6.3. Electron Localization Function

Figure 4.1 provides contour plots of the electron localization function (ELF) [57] corresponding to the atomistic structure perspectives of near-stoichiometric c -Ta₂O₅ in various charge states. From the reference stoichiometric oxide in Fig. 4.1(a), the O atoms are clearly seen as effective centers for localization of valence electron density. Note that some irregularity in the ELF is seen along the y direction in Fig. 4.1(a) because imperfect crystal symmetry leads to imperfect cross-sectioning of the equatorial O atoms in the TaO₆ and TaO₇ polyhedra. The larger ELF values and contour diameters around the cap O atoms also suggest that the cap O atoms are more effective localizers of electron density than the equatorial O atoms.

Figure 4.1(b) shows the ELF contour in a z plane that contains V_O⁰. In this case, the neighboring O atoms around V_O⁰ contract in around the vacancy which is clearly demarcated by an ELF value of nearly 1. More importantly, it is also evident that delocalization of electron density at ELF values of approximately 0.3 is observed between V_O⁰ and the three NN O atoms. This addition of delocalized electron density in the electronic structure is similar to the effect that addition of an activated donor atom has on the electronic structure of a semiconductor and consistent with the enhanced conduction observed for V_O⁰ in c -Ta₂O₅ at sufficient temperatures. First-principles studies in Al₂O₃ [12,13], TiO₂ [58], and HfO₂ [14] have shown similar delocalization effects around O vacancies to support observed σ_0 enhancement. Figures 4.1(c) and (d) show the ELF contours in a y plane that contains V_O¹⁺ and V_O²⁺, respectively. While the conductivity signatures are different for V_O¹⁺ and V_O²⁺, oxidation of V_O⁰ in both cases simply results in a void in ELF corresponding to the vacancy location. More information about V_O¹⁺ might be accessible through spin-polarized calculations, but we speculate that the essential Ta₂O_x memristor switching mechanisms are likely dominated by the $n = 0$ and $2+$ oxidation states of V_O ^{n} , while $n = 1+$ is more likely a short-lived state in a larger redox cycle. The absence of delocalized electron density for both bulk c -Ta₂O₅ and V_O²⁺ is consistent with the insulating conductivity behavior seen for both. As shown in Fig. 5.6, we found anisotropy in conductivity for c -Ta₂O_x to generally be minimal. We believe this result is a consequence of studying conductivity at the nanometer scale. At this scale, highly insulating or highly conductive regions within the supercell tend to affect the entire supercell volume, so the effect of crystal direction on nanometer-scale conductivity is negligible.

7. STATISTICAL VARIATION OF CONDUCTIVITY

Figure 7.1 shows the individual $\sigma(\omega)$ contributions from each MD configuration snapshot sampled at 0.5 ps intervals at various temperatures. As expected, considerably more noise in the $\sigma(\omega)$ distributions is observed at low temperatures. At 200K and 300K, no finite σ_0 is obtained from DFT simulation from any configuration. At 400K, two of six configurations sampled exhibit finite σ_0 . Since the log average is not robust to zero values, our $\sigma(\omega)$ values throughout this work based on a log average assigned a floor conductivity of $1 \times 10^{-30} (\Omega\text{-m})^{-1}$ in the few cases where DFT simulation produced zero σ . As the temperature is increased to 500K, all six configurations exhibit finite σ_0 over a range of nine orders of magnitude. At 700K, the range of σ_0 has shrunk to only three orders of magnitude. Finally, at 1000K, the σ_0 distribution has risen further to approximately $1 (\Omega\text{-m})^{-1}$ with a range reduced to only two orders of magnitude.

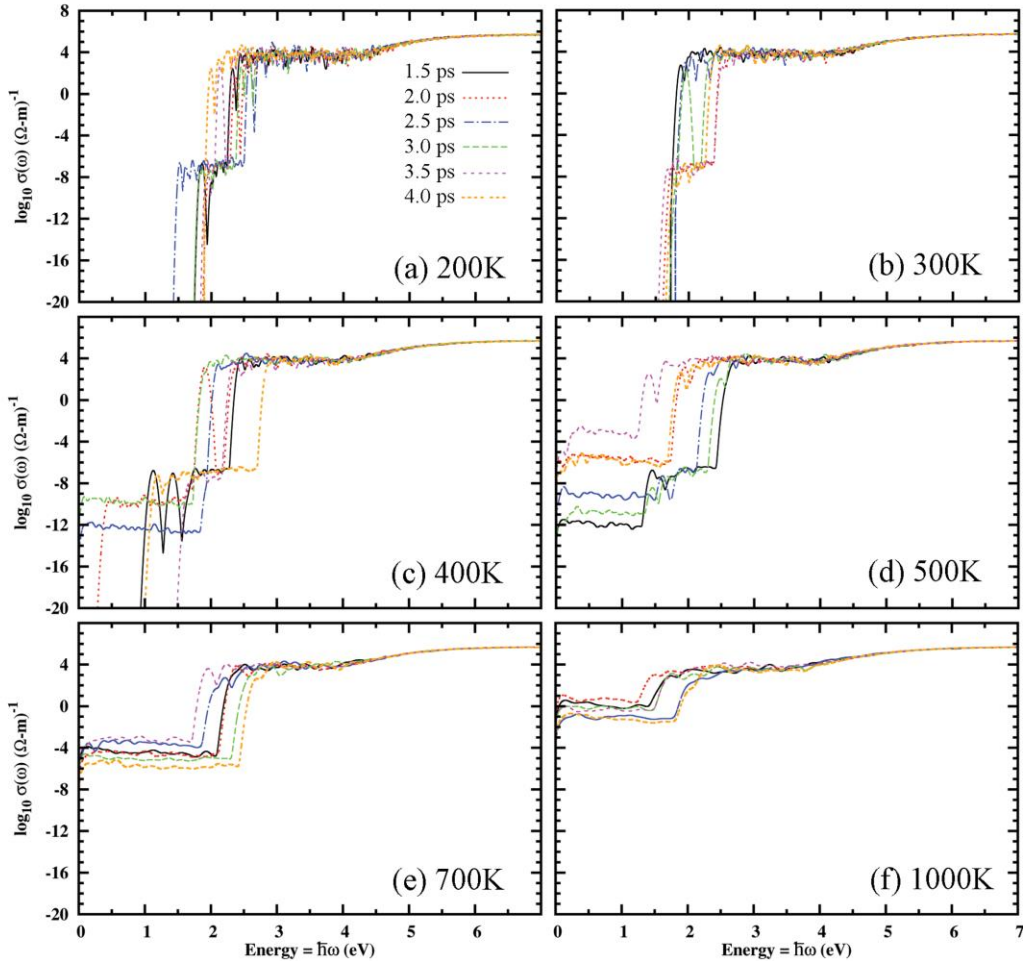


Figure 7.1. Statistical evolution of optical conductivity response for $a\text{Ta48O119} (\text{V}_\text{O}^0)$ as a function of temperature. Six $\sigma(\omega)$ curves calculated from HSE06 functionals at each temperature correspond to six MD configuration snapshots taken at 0.5 ps intervals.

In Fig. 7.2, we present σ_0 distributions for various populations at 500K. We chose 500K because conductivity calculations were generally “better behaved” and less noisy at elevated temperatures.

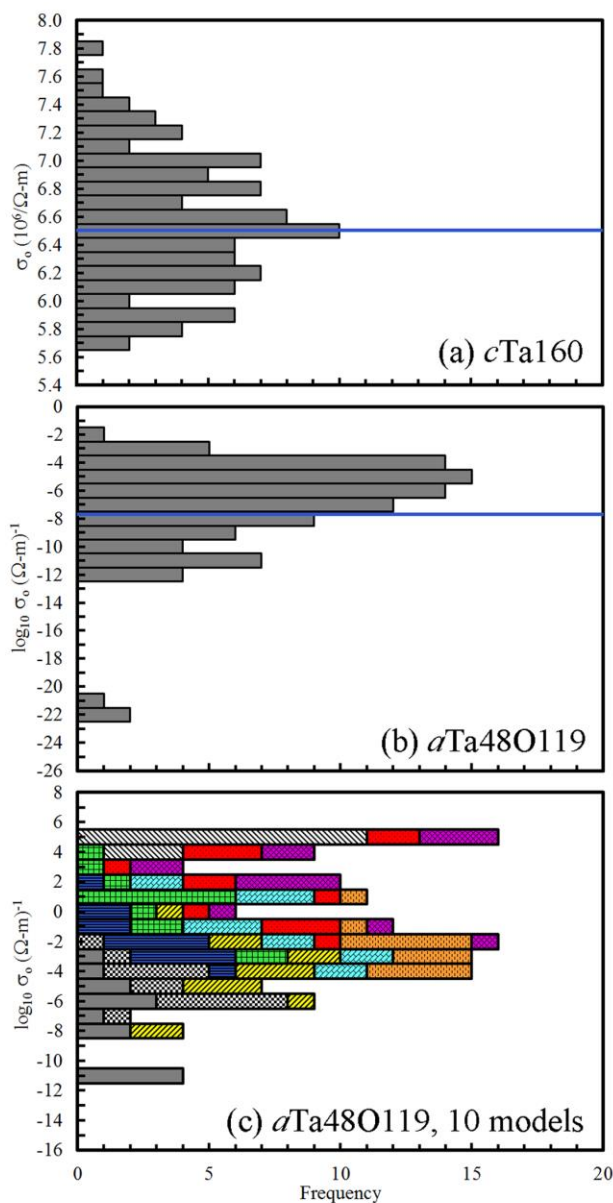


Figure 7.2. Statistical distributions sampling temporal variation of DC conductivity for (a) BCC Ta and (b) $a\text{Ta48O119}$ (V_0^0) from sampling 94 MD configuration snapshots at 0.5 ps intervals at 500K. (a) σ_0 determined with PBE functionals and blue line represents arithmetic average. (b) σ_0 determined with HSE06 functionals and blue line represents log average. Three outliers represents the minimum non-zero $\sigma(\omega > 0)$ yielded in simulation. (c) Statistical distribution of σ_0 for $a\text{Ta48O119}$ (V_0^0) from sampling 14 MD configuration snapshots across 10 different amorphous samples (140 total samples) at 500K using HSE06 functionals.

Figure 7.2(a) justifies our initial assumption that metallic populations will exhibit Gaussian distributions of conductivity using a population of $n=94$ to sample temporal variation in σ_0 . The arithmetic average illustrated for this population of $cTa160$ σ_0 values is $6.5 \times 10^6 (\Omega\text{-m})^{-1}$. Similarly, Fig. 7.2(b) justifies our assumption that insulating populations will exhibit log-normal distributions using a population of $n=94$ to sample temporal variation in σ_0 . The log average illustrated for this population of $aTa48O119$ (V_O^0) σ_0 values is $2 \times 10^{-8} (\Omega\text{-m})^{-1}$. Figure 7.2(c) further extends statistical sampling of σ_0 to include independent samples. The stacked histogram in Fig. 7.2(c) shows the σ_0 contributions from 10 independently quenched models of $aTa48O119$ in which each model was sampled with 14 MD configuration snapshots. This combination of both structural and temporal sampling of conductivity spans 16 orders of magnitude. Closer inspection of contributions reveals that some models are essentially quenched into a high conductivity configuration, while other models are quenched into a highly insulating configuration. Not surprisingly, this result suggests that better statistical predictions of σ_0 in Ta_2O_x can be obtained for the results presented herein by sampling multiple, independent configurations at each condition of composition, phase, charge state, and temperature.

This page intentionally left blank.

8. CONCLUSIONS

DFT calculations, *ab-initio* MD simulations, and the Kubo-Greenwood formula were combined to study electrical conductivity in Ta_2O_x ($0 \leq x \leq 5$) as a function of composition, phase, and temperature. We also investigated the dopant-like effect of the O monovacancy (V_O^n ; $n=0,1+,2+$) on conductivity which is commonly reported in transition metal oxides. Our conductivity results suggest that the V_O oxidation state is a critical mediator of DC conductivity (σ_0): V_O^0 behaves like an activated donor dopant with strong temperature dependence and apparent minimum σ_0 temperature threshold, while the optical conductivity response ($\sigma(\omega)$) for V_O^{2+} is nearly indistinguishable from that of stoichiometric Ta_2O_5 . This charge state dependent signature of dopant behavior in Ta_2O_x was further confirmed by the observation of occupied, shallow donor levels in the density of states for V_O^0 and visually illustrated through delocalization of electron probability density around V_O^0 in contour ELF plots. Furthermore, similar donor dopant behavior was observed in α - TiO_2 , although the apparent minimum σ_0 threshold occurs at much lower, cryogenic temperatures.

We found generally good agreement between our DFT conductivities and experimental measurements on both Ta_2O_x thin films and powder-sintered Ta_2O_5 pellets, although simulation errors were largest for the stoichiometric oxide. DFT total energy calculations in the crystalline phase found that V_O^0 prefers equatorial O sites, while V_O^{1+} and V_O^{2+} are energetically preferred in the O cap sites of TaO_7 polyhedra. Contrary to expectations, a change of sign in the thermal coefficient of resistivity was observed simply by amorphization of BCC Ta, so no metal-insulator-transition was observed in the intermediate α - Ta_2O_x compositions. While our first-principles study of electrical conductivity found only subtle spatial anisotropy in σ_0 , large temporal and structural variations (16 orders of magnitude) in σ_0 for a single amorphous composition stress the importance of adequate statistical sampling to ensure reliable DFT property predictions. Our work provides a foundation for further study of the various conduction mechanisms responsible for Ta_2O_x conductivity as a function of composition.

This page intentionally left blank.

9. REFERENCES

1. R. Bassiri, K. B. Borisenko, D. J. H. Cockayne, J. Hough, I. MacLaren, and S. Rowan, *Appl. Phys. Lett.* **98**, 031904 (2011).
2. R. Ramprasad, *J. Appl. Phys.* **94**, 5609 (2003).
3. R. Ramprasad, *J. Appl. Phys.* **95**, 954 (2004).
4. J. J. Yang, M.-X Zhang, J. P. Strachan, F. Miao, M. D. Pickett, R. D. Kelley, G. Medeiros-Ribeiro, and R. S. Williams, *Appl. Phys. Lett.* **97**, 232102 (2010).
5. J. P. Strachan, G. Medeiros-Ribeiro, J. J. Yang, M.-X Zhang, F. Miao, I. Goldfarb, M. Holt, V. Rose, and R. S. Williams, *Appl. Phys. Lett.* **98**, 242114 (2011).
6. M.-J. Lee, C. B. Lee, D. Lee, S. R. Lee, M. Chang, J. H. Hur, Y.-B. Kim, C.-J. Kim, D. H. Seo, S. Seo, U.-I. Chung, I.-K. Yoo, and K. Kim, *Nature Materials* **10**, 625 (2011).
7. F. Miao, J. P. Strachan, J. J. Yang, M.-X. Zhang, I. Goldfarb, A. C. Torrezan, P. Eschbach, R. D. Kelley, G. Medeiros-Ribeiro, and R. S. Williams, *Adv. Mat.* **23**, 5633 (2011).
8. F. Miao, W. Yi, I. Goldfarb, J. J. Yang, M.-X. Zhang, M. D. Pickett, J. P. Strachan, G. Medeiros-Ribeiro, and R. S. Williams, *ACS Nano* **6**, 2312 (2012).
9. D. B. Strukov, G. S. Snider, D. R. Stewart, and R. S. Williams, *Nat. Lett.* **453**, 80 (2008).
10. R. S. Williams, *IEEE Spectrum* **45**, 28 (2008).
11. R. Waser, R. Dittmann, G. Staikov, and K. Szot, *Adv. Mat.* **21**, 2632 (2009).
12. H. Momida, S. Nigo, G. Kido, and T. Ohno, *Appl. Phys. Lett.* **98**, 042102 (2011).
13. S. Nigo, M. Kubota, Y. Harada, T. Hirayama, S. Kato, H. Kitazawa, and G. Kido, *J. Appl. Phys.* **112**, 033711 (2012).
14. Z. Wang, H. Y. Yu, X. A. Tran, Z. Fang, J. Wang, and H. Su, *Phys. Rev B* **85**, 195322 (2012).
15. Q. Xia, W. Robinett, M. W. Cumbie, N. Banerjee, T. J. Cardinali, J. J. Yang, W. Wu, X. Li, W. M. Tong, D. B. Strukov, G. S. Snider, G. Medeiros-Ribeiro, and R. S. Williams, *Nano Lett.* **9**, 3640 (2009).
16. P. N. Baker, *Thin Sol. Films* **14**, 3 (1972).
17. J. E. Nestell, Jr., K. J. Scoles, and R. W. Christy, *J. Appl. Phys.* **53**, 8993 (1982).

18. R. M. Fleming, D. V. Lang, C. D. W. Jones, M. L. Steigerwald, D. W. Murphy, G. B. Alers, Y.-H. Wong, R. B. van Dover, J. R. Kwo, and A. M. Sergent, *J. Appl. Phys.* **88**, 850 (2000).
19. N. N. Iosad, G. J. Ruis, E. V. Morks, A. F. Morpurgo, N. M. van der Pers, P. F. A. Alkemade, and V. G. M. Sivel, *J. Appl. Phys.* **95**, 8087 (2004).
20. R. Nakamura, K. Tanaka, M. Ishimaru, K. Sato, T. J. Konno, and H. Nakajima, *Scripta Materialia* **66**, 182 (2012).
21. S. Gnanarajan, S. K. H. Lam, and C. P. Foley, *J. Appl. Phys.* **101**, 063535 (2007).
22. I. Goldfarb, F. Miao, J. J. Yang, W. Yi, J. P. Strachan, M.-X. Zhang, M. D. Pickett, G. Medeiros-Ribiero, and R. S. Williams, *Appl. Phys. A* **107**, 1 (2012).
23. S. P. Garg, N. Krishnamurthy, A. Awasthi, and M. Venkatraman, *J. Phase Equil.* **17**, 63(1996).
24. G. L. Brennecka and D. A. Payne, *J. Am. Ceram. Soc.* **89**, 2089 (2006).
25. I. E. Grey, W. G. Mumme, and R. S. Roth, *J. Sol. State Chem.* **178**, 3308 (2005).
26. M. V. Ivanov, T. V. Perevalov, V. S. Aliev, V. A. Gritsenko, and V. V. Kaichev, *J. Appl. Phys.* **110**, 024115 (2011).
27. N. C. Stephenson and R. S. Roth, *Acta. Cryst.* **B27**, 1037 (1971).
28. H. Sawada and K. Kawakami, *J. Appl. Phys.* **86**, 956 (1999).
29. W. Andreoni and C. A. Pignedoli, *Appl. Phys. Lett* **96**, 062901 (2010).
30. Y.-N. Wu, L. Li, and H.-P. Cheng, *Phys. Rev. B* **83**, 144105 (2011).
31. R. Kubo, *J. Phys. Soc. Jpn.* **12**, 570 (1957).
32. D. A. Greenwood, *Proc. Phys. Soc.* **71**, 585 (1958).
33. N. F. Mott and E. A. Davis, *Electronic Processes in Non-Crystalline Materials*, 2nd ed. (Oxford Univ. Press, Oxford, 1979).
34. M. P. Desjarlais, J. D. Kress, and L. A. Collins, *Phys. Rev. E* **66**, 025401R (2002).
35. M. Pozzo, M. P. Desjarlais, and D. Alfè, *Phys. Rev. B* **84**, 054203 (2011).
36. D. Alfè, M. Pozzo, and M. P. Desjarlais, *Phys. Rev. B* **85**, 024102 (2012).
37. Y. Laudernet, J. Clérouin, and S. Mazevet, *Phys. Rev. B* **70**, 165108 (2004).

38. J. Cl rouin, Y. Laudernet, V. Recoules, and S. Mazevet, *Phys. Rev. B* **72**, 155122 (2005).
39. T. R. Mattsson and M. P. Desjarlais, *Phys. Rev. Lett.* **97**, 017801 (2006).
40. M. French, T. R. Mattsson, and R. Redmer, *Phys. Rev. B* **82**, 174108 (2010).
41. G. Kresse and J. Hafner, *Phys. Rev. B* **47**, 558 (1993); **49**, 14251(1994); G. Kresse and J. Furthm ller, *Comp. Mater. Sci.* **6**, 15 (1996); *Phys. Rev. B* **54**, 11169 (1996).
42. G. Kresse and J. Furthm ller, *VASP the Guide* (Vienna University of Technology, Vienna, 2001).
43. P. E. Bl chl, *Phys. Rev. B* **50**, 17953 (1994).
44. J. P. Perdew, K. Burke, and M. Ernzerhof, *Phys. Rev. Lett.* **77**, 3865 (1996).
45. J. Heyd, G. E. Scuseria, and M. Ernzerhof, *J. Chem. Phys.* **118**, 8207 (2003); **124**, 219906 (2006).
46. J. Heyd and G. E. Scuseria, *J. Chem. Phys.* **121**, 1187 (2004).
47. *CRC Handbook of Chemistry and Physics, 92nd ed.*, edited by W. M. Haynes (CRC Press, Boca Raton, FL, 2011).
48. R. J. Bondi, S. Lee, and G. S. Hwang, *Phys. Rev. B* **81**, 195207 (2010).
49. A. Udyansky, J. von Pezold, A. Dick, and J. Neugebauer, *Phys. Rev. B* **83**, 184112 (2011).
50. M. Methfessel and A. T. Paxton, *Phys. Rev. B* **40**, 3616 (1989).
51. J. D. Jackson, *Classical Electrodynamics, 2nd ed.* (Wiley, New York, 1975).
52. V. A. Gopar, K. A. Muttalib, and P. W lfle, *Phys. Rev. B* **66**, 174204 (2002).
53. P. Marko , *Phys. Rev. Lett.* **83**, 588 (1999).
54. V. A. Gopar and R. A. Molina, *Phys. Rev. B* **81**, 195415 (2010).
55. G. S. Oehrlein, *J. Appl. Phys.* **59**, 1587 (1986).
56. A. Janotti, J. B. Varley, P. Rinke, N. Umezawa, G. Kresse, and C. G. Van de Walle, *Phys. Rev. B* **81**, 085212 (2010).
57. B. Silvi and A. Savin, *Nature* **371**, 683 (1994).
58. S.-G. Park, B. Magyari-K pe, and Y. Nishi, *IEEE Elec. Dev. Lett.* **32**, 197 (2011).

DISTRIBUTION

1	MS1084	M. Marinella	1748
2	MS1159	R. J. Bondi	1344
1	MS1159	J. K. McDonald	1344
1	MS1159	J. W. Bryson	1344
1	MS1167	E. F. Hartman	1343
1	MS1167	M. L. McLain	1343
1	MS1179	L. Lorence	1341
1	MS1179	G. S. Heffelfinger	1300
1	MS1189	M. P. Desjarlais	1600
1	MS1322	A. P. Thompson	1426
1	MS1411	G. L. Brennecka	1816
1	MS0899	Technical Library	9536 (electronic copy)
1	MS0359	D. Chavez, LDRD Office	7911

